

Modeling of two-layer eddies and coastal flows with a particle method

Oleg E. Esenkov

Rosenstiel School of Marine and Atmospheric Science, University of Miami, Miami

Benoit Cushman-Roisin

Thayer School of Engineering, Dartmouth College, Hanover, New Hampshire

Abstract. An existing particle-in-cell (PIC) numerical method developed for the study of two-layer mesoscale motions with outcropping pycnocline is applied to lens-like anticyclonic vortices and buoyant coastal currents. From a first series of experiments investigating the evolution of an initially elongated lens-like anticyclone, it is found that motions induced in the lower layer act only to increase the rotation of the vortex structure and do not appear to affect the process of eccentricity reduction (partial axisymmetrization). Eccentricity reduction, if any, produces a final vortex of aspect ratio between 1.8 and 1.9, a value that is very close to the stability threshold of large, reduced-gravity lenses. A second series of experiments devoted to vortex mergers determines how the maximal separation distance for which two circular anticyclonic lenses merge spontaneously varies with vortex size (ratio of lens radius to deformation radius) and stratification (ratio of lens central thickness to ocean depth). A third series of experiments considers the interaction of a lens vortex in the upper layer with a potential-vorticity anomaly in the lower layer. “Second-hand” relative vorticity, generated in the lower layer under the action of vertical stretching induced by the movement of the upper-layer vortex, interacts with “first-hand” relative vorticity, created by the existing potential-vorticity, to create effects similar to those predicted by studies of two-layer point vortices (hetons). Finally, the PIC method is generalized to simulate the finite-amplitude instability of a buoyant geostrophic/hydrostatic intrusion flowing along a vertical coastal wall. Those results, however, are reported here more as a demonstration on how the PIC method can be extended to include coastal boundaries than as a thorough investigation of coastal-current instabilities.

1. Introduction

A substantial portion of the ocean’s energy is contained in the so-called mesoscale activity, the internal weather of the sea. These motions, with length scales of the order of the first baroclinic radius of deformation (20–200 km), are mostly composed of jets and vortices [Robinson, 1983]. Their length scale implicates geostrophy, and, consequently, their relative high velocities are accompanied by substantial vertical displacements of density surfaces, causing on numerous occasions their outcrop through the surface. Examples are the north wall of the Gulf Stream, the periphery of its detached rings, the offshore edge of coastal intrusions, and upwelling fronts. We shall use here the word “front” to describe the surface outcropping of a pycnocline or, in the context of a layered model, the surfacing of a density interface. Indeed, such outcropping causes important horizontal density gradients along the surface and corresponds to a frontal zone.

Since geostrophy places a high degree of relation between horizontal density gradients and velocities (via the thermal-wind balance), fronts are accompanied by flow fields that are highly sheared in the horizontal and thus subject to barotropic instability, while the sloping density surfaces contain available

potential energy susceptible of being released by baroclinic instability. As a result, mesoscale frontal systems are replete with transient motions.

Outcropping of density surfaces, however, creates severe problems for the modeler. In a system modeled with continuous stratification, the close packing of density surfaces necessitates high resolution in both horizontal and vertical directions, which, because of the wandering nature of the front, needs to be implemented over large areas of the computational domain. Insufficient resolution causes undesirable diffusion and acts to smear the front over time. On occasions, computational limitations have led to sacrifice variation in one horizontal direction for the benefit of high resolution in the vertical [e.g., Adamec and Elsberry, 1985]. In contrast, layered models with outcropping interface(s) allow true discontinuities but at the cost of different sets of equations on opposite sides of outcrop lines (fewer equations on the side where there is one less active layer). As a result, much of the present knowledge on frontal instabilities has been derived from theoretical studies. However, these typically rely on a host of simplifying assumptions such as infinitesimal-amplitude perturbations on a simple basic state [e.g., Paldor and Ghil, 1990, and references therein] or asymptotic dynamics [Stern, 1980; Cushman-Roisin, 1986].

Numerical investigations of frontal instabilities based on layered models have traditionally avoided outcrops, even for fron-

Copyright 1999 by the American Geophysical Union.

Paper number 1999JC900043.
10148-0227/99/1999JC900043\$09.00

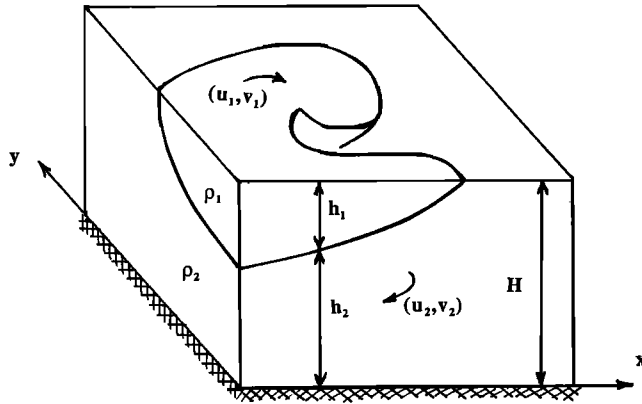


Figure 1. Sketch of an unsteady two-layer system with outcropping and the attending notation.

tal studies (e.g., quasi-geostrophic study of *Pratt and Stern* [1986]), thus overlooking crucial dynamics. A most important exception is the isopycnic model using the flux-corrected transport (FCT) scheme [*Sun et al.*, 1993, and references therein]. Thusfar, this model has only been applied to large-scale circulation problems, where outcrops of density interfaces arise from the finite vertical displacement of the thermocline over the meridional extent of the ocean basin.

An alternative, specifically designed for the simulation of mesoscale-front variability, is the particle-in-cell (PIC) method. This method was originally developed for free-surface problems in fluid dynamics, then applied to plasma physics and astrophysics [*Hockney and Eastwood*, 1988] and later adapted to oceanography [*Pavia and Cushman-Roisin*, 1988, 1990]. It combines both Lagrangian and Eulerian approaches, treating each part of the model by the representation that fits it best. Typically, the field variables, such as pressure and layer thickness, are evaluated on a fixed Eulerian mesh (forming the cells), while the variables that are naturally attached to particles, such as velocities, accelerations, and forces, are calculated in a Lagrangian fashion.

A critical procedure in the model is the transfer, at least once each way per time step, of information between the particles and the grid. Particle information is mapped onto the grid by tallying characteristics of the particles in each cell; this leads to relative weights binding (for that time step only) every particle to its neighboring grid points; these weights are used again later to interpolate gridded information at the particle locations during the reverse information transfer (for details, see *Pavia and Cushman-Roisin* [1988] and *Cushman-Roisin et al.* [1999]). The chief advantage of the PIC method is its avoidance of tracking the outcropping line as it moves and distorts in time. In the model, the front is simply the envelope of the group (or groups) of particles, which is easily perceived by the eye upon the examination of a plot but which never needs to be constructed by the computer code.

Pavia and Cushman-Roisin [1988] developed the essential characteristics of the particle-in-cell algorithm for mesoscale oceanography. They, however, limited the physics to a reduced-gravity model in the asymptotic regime of the frontal-geostrophic dynamics (length scales substantially longer than the deformation radius). This restriction was later removed [*Pavia and Cushman-Roisin*, 1990], and the primitive-equation model version was used to investigate the merging of anticy-

clonic lens-like vortices with particular attention paid to the filamentation process and the formation of satellite vortices. The model, however, retained a single moving layer and was therefore deprived of baroclinic instability. Extension to two moving layers was done by *Mathias* [1992], and the incorporation of a lateral boundary (such as a coast) was later accomplished by *Esenkov* [1994]. A detailed description of the method and of its performance are given by *Cushman-Roisin et al.* [1999].

The purpose of the present article is to demonstrate the flexibility and usefulness of the two-layer PIC method in simulating various mesoscale frontal dynamics. Of particular interest are the behavior of elongated vortices, vortex interactions such as merging, and the variability of coastal currents with offshore front.

2. Model

We consider a two-layer system of inviscid and incompressible fluid with constant densities ρ_1 and ρ_2 on a flat bottom (Figure 1). (Extension to irregular bottom topography is straightforward.) The shallow-water equations that describe the motion of such system are:

$$\frac{\partial u_i}{\partial t} + u_i \frac{\partial u_i}{\partial x} + v_i \frac{\partial u_i}{\partial y} - f v_i = -\frac{1}{\rho_0} \frac{\partial p_i}{\partial x} \quad (1)$$

$$\frac{\partial v_i}{\partial t} + u_i \frac{\partial v_i}{\partial x} + v_i \frac{\partial v_i}{\partial y} + f u_i = -\frac{1}{\rho_0} \frac{\partial p_i}{\partial y} \quad (2)$$

$$\frac{\partial h_i}{\partial t} + \frac{\partial(h_i u_i)}{\partial x} + \frac{\partial(h_i v_i)}{\partial y} = 0 \quad (3)$$

where the subscript $i = 1, 2$ indicates the upper and lower layer, respectively; p_i , h_i , and (u_i, v_i) are the pressure, thickness, and velocity components in each layer. The Coriolis parameter, f , may in general be a function of the horizontal coordinates (x, y) but will be taken as a constant here.

Equations (1)–(3) are completed by a geometric relation and the hydrostatic balance:

$$h_1 + h_2 = H \quad (4)$$

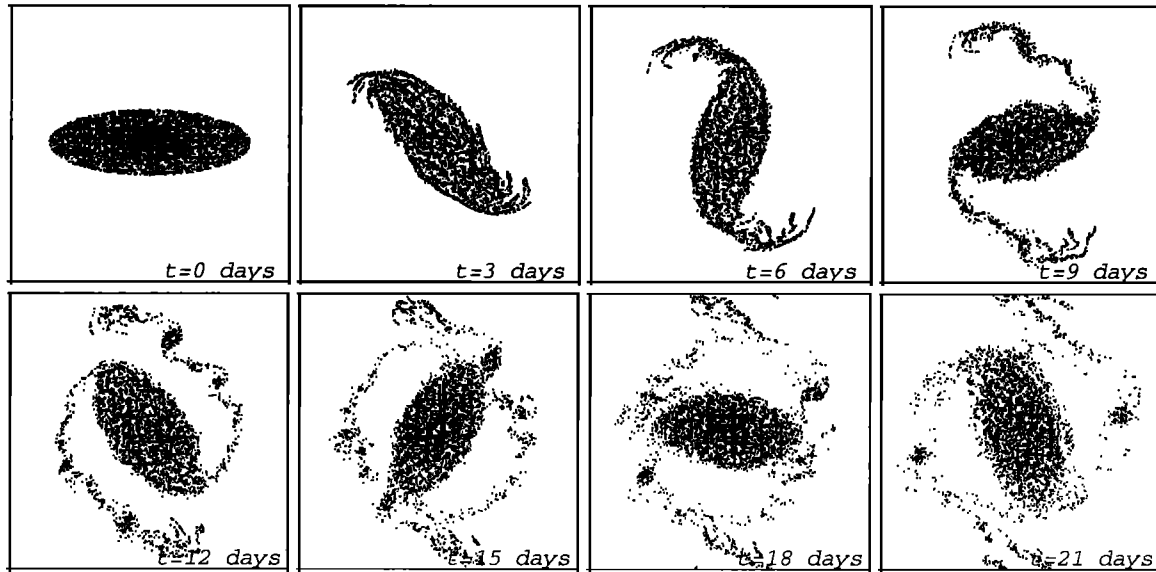
$$p_1 = p_2 + \rho_0 g' h_1 \quad (5)$$

In these last equations, H is the total depth of the fluid, and g' the reduced gravity [$g' = g(\rho_2 - \rho_1)/\rho_2$]. Because the free-surface vertical elevations are much smaller than those of the interface separating the two layers, we use the rigid-lid approximation, which eliminates surface gravity waves. If we furthermore assume a flat bottom, the total depth H is constant.

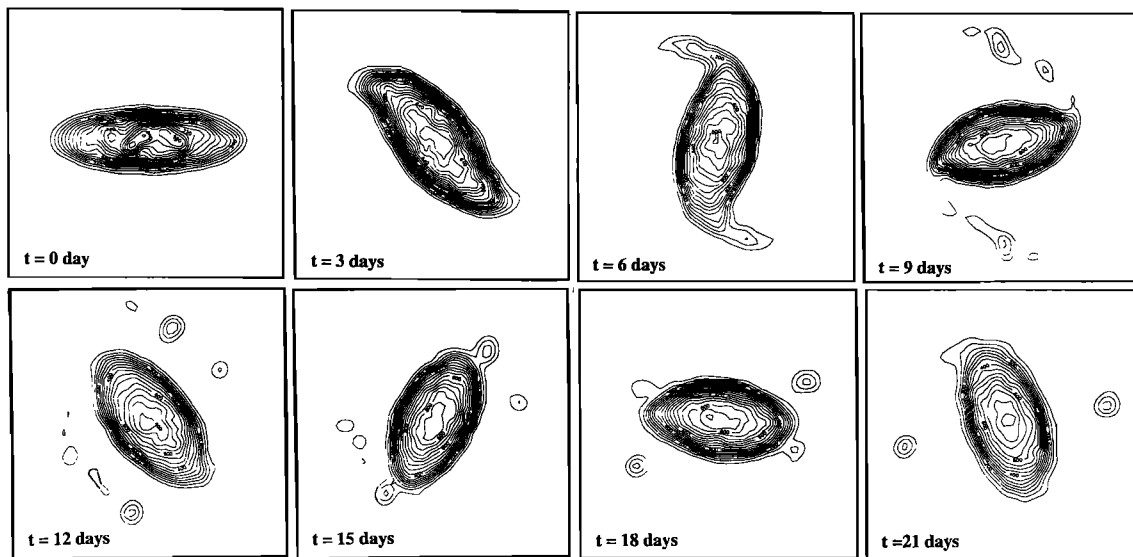
Because the lower layer typically encompasses a much deeper part of the ocean than the upper layer (several thousand meters versus a few hundred meters), the thickness variations in the lower layer are relatively small, and a quasi-geostrophic approximation can be used to describe its dynamics. It can be shown [*Mathias*, 1992] that application of the approximation to (1)–(5) results in the reduction of the governing equations to

$$\frac{\partial u_1}{\partial t} + u_1 \frac{\partial u_1}{\partial x} + v_1 \frac{\partial u_1}{\partial y} - f v_1 = -\frac{1}{\rho_0} \frac{\partial p_1}{\partial x} \quad (6)$$

$$\frac{\partial v_1}{\partial t} + u_1 \frac{\partial v_1}{\partial x} + v_1 \frac{\partial v_1}{\partial y} + f u_1 = -\frac{1}{\rho_0} \frac{\partial p_1}{\partial y} \quad (7)$$



(a)



(b)

Figure 2. Evolution of an initially elliptical lens-like vortex: (a) particle positions and (b) upper-layer thickness contours every 3 days. The parameter values are $\alpha = \sqrt{ab}/R_d = 5.0$, $\gamma = a/b = 3.0$, and $\delta = H_1/H = 0.25$. For the sake of these plots, the dimensionless time used in the numerical code (scaled by $1/f$) was converted into a dimensional time with $f = 10^{-4} \text{ s}^{-1}$. Note the filamentation and eccentricity reduction of the main vortex.

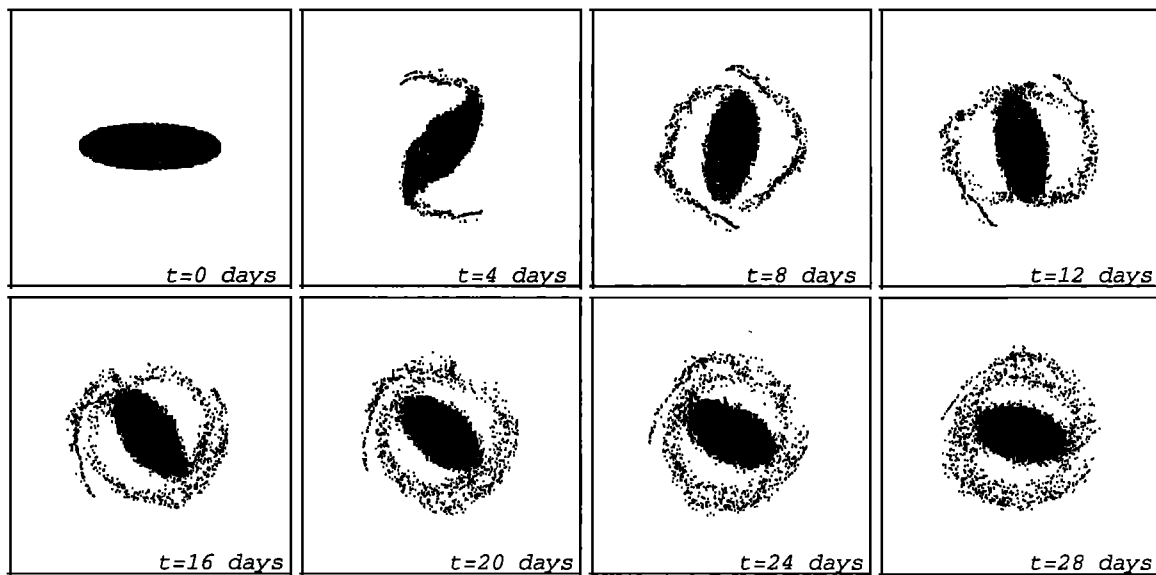
$$\frac{\partial h_1}{\partial t} + \frac{\partial(h_1 u_1)}{\partial x} + \frac{\partial(h_1 v_1)}{\partial y} = 0 \quad (8)$$

$$\frac{\partial q_2}{\partial t} + \frac{1}{\rho_0 f} J(p_2, q_2) = 0 \quad (9)$$

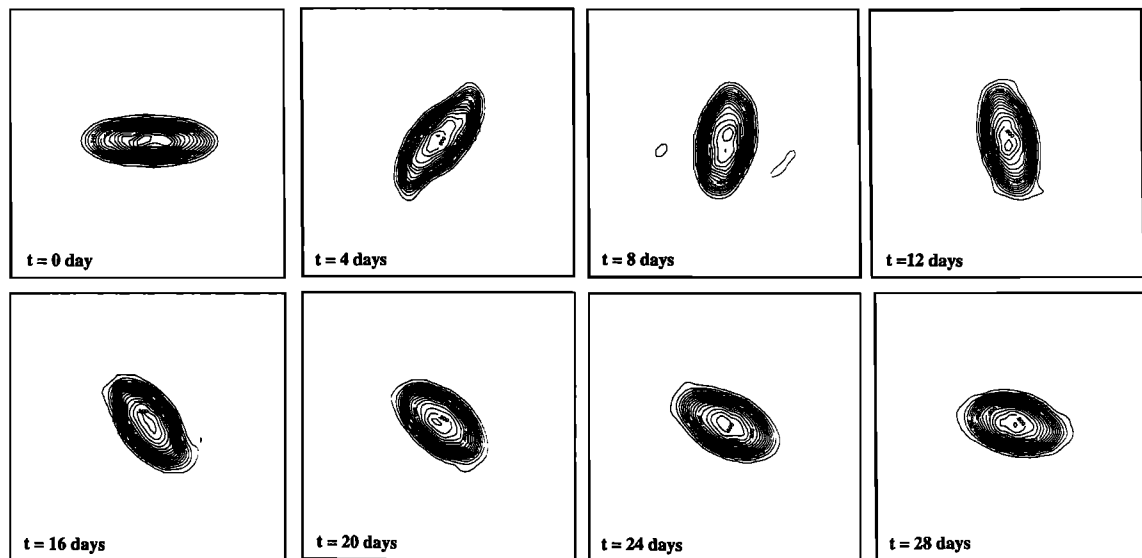
$$q_2 = \frac{1}{\rho_0 f} \nabla^2 p_2 + \frac{f}{H} h_1 \quad (10)$$

$$p_1 = p_2 + \rho_0 g' h_1 \quad (11)$$

in which we recognize the set of primitive equations for the upper layer (Equations (6)–(8)) and a single prognostic equation for the lower-layer potential vorticity q_2 (Equation (9), where $J(a, b)$ is the traditional Jacobian operator). Note how the dynamics of the two layers are twice coupled: once in the stretching and squeezing of the lower layer via the variation of the upper-layer thickness (h_1 term in Equation (10)), and once again in the lower-layer pressure field adding to the upper-layer pressure via the hydrostatic balance (p_2 term in Equation



(a)



(b)

Figure 3. Same as for Figure 2, except that the initial vortex is smaller, with $\alpha = \sqrt{ab}/R_d = 3.5$: (a) particle positions and (b) upper-layer thickness contours every 4 days. Note that the eccentricity reduction proceeds more rapidly than in the case shown in Figure 2.

(11)). The two layers are thus fully interacting despite the quasi-geostrophic reduction of the dynamics in one of the two.

The PIC method is fully described by *Cushman-Roisin et al.* [1999] and is only briefly summarized here. The upper-layer fluid is dissected into a large number of material particles, and every particle is assigned a volume, which remains constant, a vector position, and a vector velocity, which both vary over time. In contrast, the lower layer is represented by a gridded distribution of its potential vorticity. Because all particles retain their volume, no volume is gained or lost, and the upper-layer continuity equation, (8), is automatically satisfied. The position is updated in time by the velocity, while the velocity

is updated by Newton's law (mass \times acceleration = sum of forces). There are two forces: the Coriolis force (which is easily included, since it is an immediate function of the particle's velocity and of its position if the Coriolis parameter is spatially varying) and the pressure-gradient force (which is the chief difficulty because it is through it that particles interact with one another). To calculate the pressure-gradient force, the method calculates first the upper-layer thickness h_1 on a fixed square grid as the total volume of particles in a grid cell divided by the cell area. Next, it determines the upper and lower pressure distributions on the same grid: p_2 by integration of (10) from the current potential-vorticity q_2 and the just acquired thick-

ness field h_1 and then p_1 by the hydrostatic balance (11). Next, (9) is used to march q_2 in time. Finally, the gradient of p_1 is calculated on the grid and interpolated at the particle sites, providing the pressure-gradient force on every particle. The Jacobian operator in (9) is discretized according to the Arakawa scheme B [Arakawa and Mesinger, 1976], while the updating of positions and velocities is performed with an Adams-Bashforth scheme [Schwarz, 1989]. The time step is chosen so that no particle is moved in a single step over a distance greater than one tenth of the grid size.

3. Vortex Simulations

3.1. Initialization of a Vortex

To initialize particles in a vortex formation, we proceed as follows: We first fill a unit circle ($\sqrt{x^2 + y^2} = r \leq 1$) with N particles located at random, ascribing to particle k the coordinates

$$x_k = r_k \cos \theta_k \quad y_k = r_k \sin \theta_k \quad (12a)$$

$$r_k = \sqrt{n_1} \quad \theta_k = 2\pi n_2 \quad (12b)$$

where (n_1, n_2) is the k th pair in a series of random numbers between 0 and 1. The square root of n_1 forces more particles to lie at larger radii in order to achieve a uniform distribution over the unit circle. We then assign a volume to every particle so as to impose a parabolic thickness profile of unit center depth and vanishing thickness at unit radius [$h_1(r) = 1 - r^2$, $0 \leq r \leq 1$]. By virtue of the uniform distribution, every particle is expected to occupy the same fraction π/N of the unit-circle area, and the volume assigned to the k th particle is thus the product of the layer thickness at radius r_k by the horizontal area π/N that it occupies:

$$V_k = \frac{\pi(1 - r_k^2)}{N} \quad (13)$$

The next step is to assign to the vortex its actual horizontal and vertical dimensions by dimensionalizing the particle volumes

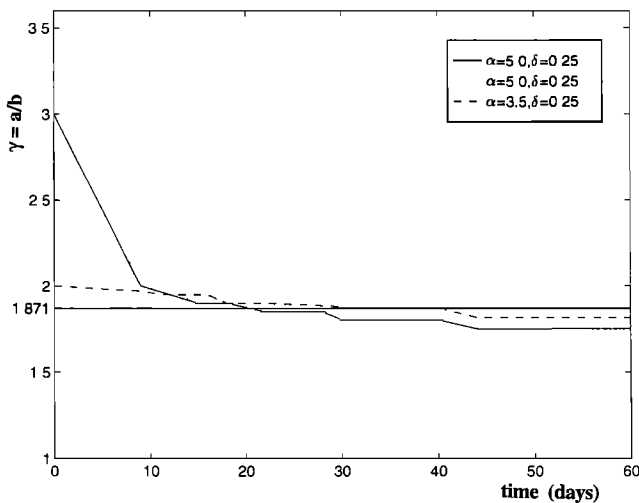


Figure 4. Evolution of the eddy aspect ratio a/b during eccentricity reduction, for several simulations as indicated along the curves. All ratios stabilize not too far from 1.871, although this critical value was established only for large, reduced-gravity vortices (limit $\alpha \gg 1$ and $\delta = 0$).

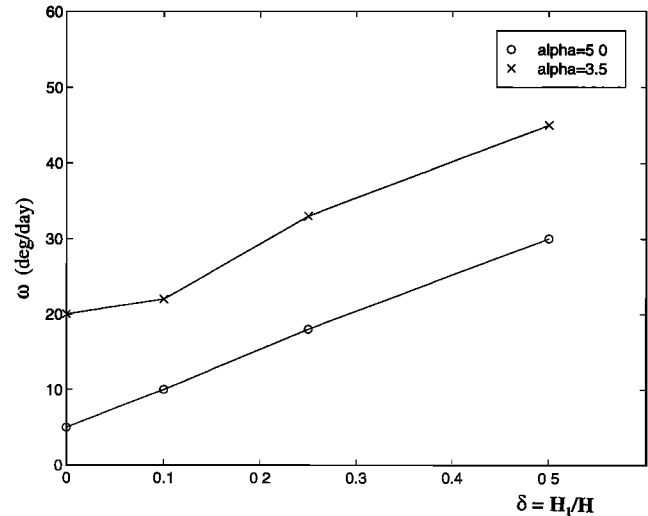


Figure 5. Variation of the angular rotation rate of stabilized elliptical vortices versus vortex size ($\alpha = \sqrt{ab}/R_d$) and layer-depth ratio ($\delta = H_1/H$). As for Figures 2 and 3, dimensional time is recovered by use of $f = 10^{-4} \text{ s}^{-1}$.

and position coordinates appropriately. If an elliptical vortex is desired, distinct amounts of stretching are used for the x and y coordinates. For a central depth H_1 , semimajor axis a , and semiminor axis b , i.e.,

$$h_1 = H_1 \left(1 - \frac{x^2}{a^2} - \frac{y^2}{b^2} \right) \quad (14)$$

all volumes are multiplied by abH_1 , x coordinates are multiplied by a , and y coordinates are multiplied by b . Finally, every particle is assigned an initial velocity. To avoid large transient motions that would result from an initial state greatly out of equilibrium, we choose the velocity field that would yield gradient-wind balance in the reduced-gravity limit:

$$u_k = +\omega_x y_k \quad v_k = -\omega_y x_k \quad (15)$$

where the constants ω_x and ω_y are obtained by substitution of the preceding expressions in (6) and (7), together with $\partial/\partial t = 0$, $p_2 = 0$, and $h_1 = H_1[1 - (x/a)^2 - (y/b)^2]$:

$$\frac{\omega_x}{f} = \frac{1}{2} - \frac{R_d^2}{a^2} + \frac{R_d^2}{b^2} - \sqrt{\left(\frac{R_d^2}{a^2} - \frac{R_d^2}{b^2} \right)^2 - \left(\frac{R_d^2}{a^2} + \frac{R_d^2}{b^2} \right) + \frac{1}{4}} \quad (16a)$$

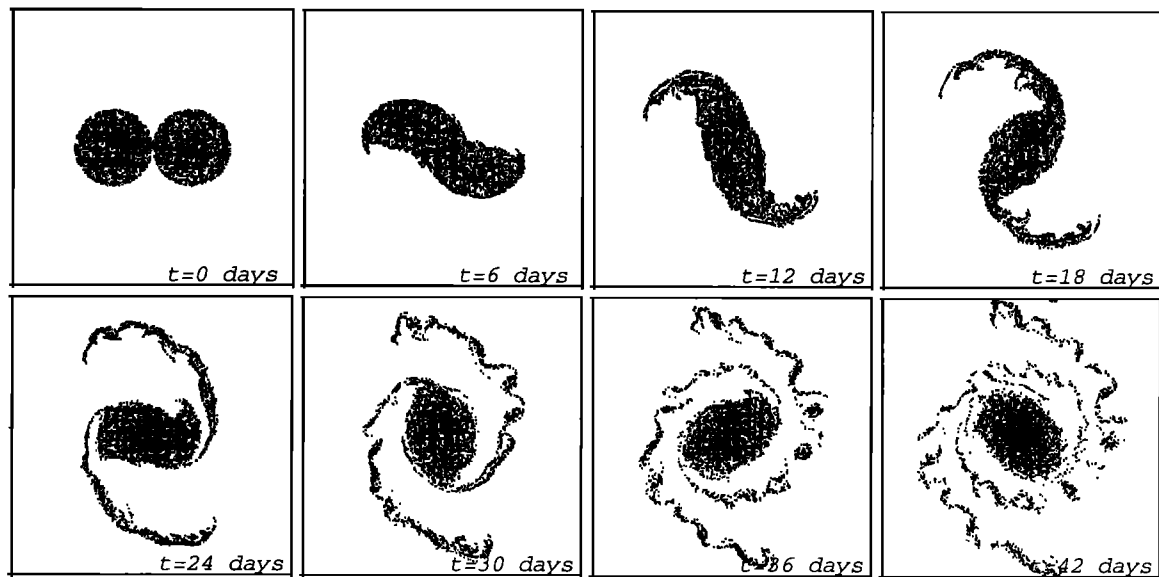
$$\frac{\omega_y}{f} = \frac{1}{2} + \frac{R_d^2}{a^2} - \frac{R_d^2}{b^2} - \sqrt{\left(\frac{R_d^2}{a^2} - \frac{R_d^2}{b^2} \right)^2 - \left(\frac{R_d^2}{a^2} + \frac{R_d^2}{b^2} \right) + \frac{1}{4}} \quad (16b)$$

In these expressions appears the internal deformation radius $R_d = \sqrt{g'H_1}/f$.

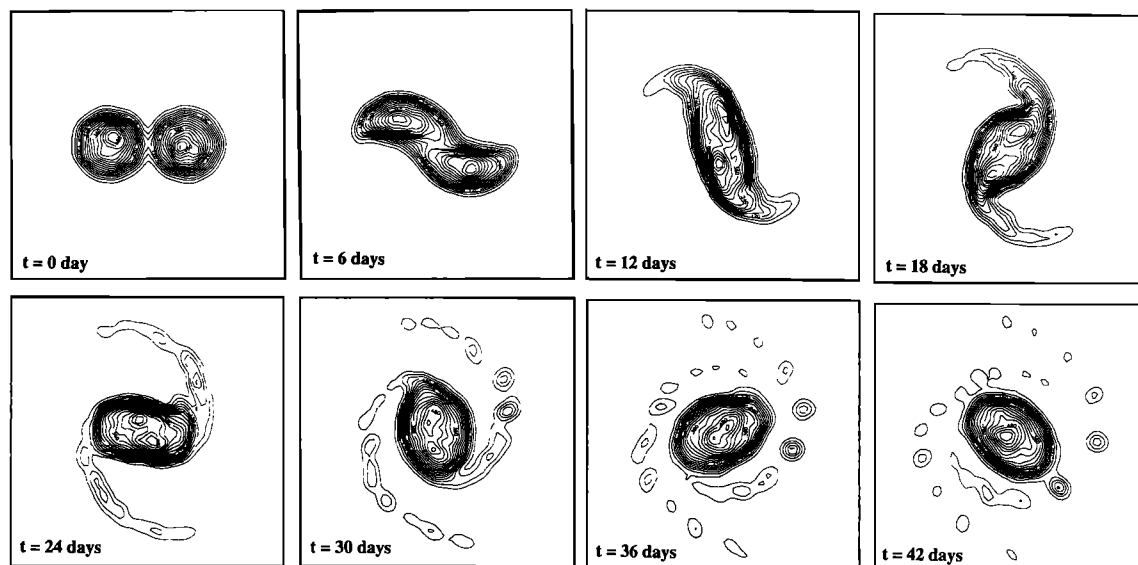
The initial lower-layer potential vorticity q_2 is simply a gridded sample of a given analytical function (equals 0 in most experiments). In all runs, we use $N = 5000$ particles per vortex and a 60×60 square grid, on which we impose doubly periodic boundary conditions.

3.2. Partial Axisymmetrization of Elliptical Vortices

The purpose of this first series of experiments is to study the evolution of elliptical vortices in a two-layer model. Satellite



(a)



(b)

Figure 6. Merging of two identical upper-layer anticyclonic lenses: (a) particle positions and (b) upper-layer thickness contours every 6 days. Parameters are $\alpha = R/R_d = 5.0$, $\lambda = d/R = 2.0$, and $\delta = H_1/H = 0.25$. As for Figures 2 and 3, the dimensionless time used in the numerical code (scaled by $1/f$) was converted into a dimensional time with $f = 10^{-4} \text{ s}^{-1}$. Note the formation of filaments and their subsequent instability, the eccentricity reduction of the merged core, and its clockwise rotation.

observations of the sea surface [Evans *et al.*, 1985, and references therein] and in situ measurements [e.g., Richardson *et al.*, 1973] have consistently shown that Gulf Stream rings are more or less circular, occasionally having a very moderate eccentricity. There are, however, several reasons to believe that elongated eddies should occur in the ocean. The two primary reasons are nonaxisymmetric birthing condition and subsequent distortion in the presence of shearing currents. We may therefore hypothesize that vortices tend to resist high degrees of eccentricity and to evolve spontaneously into less eccentric structures.

Several numerical and analytical investigations have provided partial answers. Love [1893] found that vortices of the two-dimensional Euler equations are stable if their aspect ratio $a/b < 3$ and are unstable at greater eccentricities. Cushman-Roisin [1986] subjected the long length-scale limit of the reduced-gravity elliptical vortex [Cushman-Roisin *et al.*, 1985] to a small-amplitude stability analysis and demonstrated for this case too that moderately elongated eddies are stable while highly eccentric vortices are unstable. The threshold aspect ratio is $\sqrt{7/2} = 1.871$. Ripa [1987] extended the analysis to any length scale to arrive essentially at the same conclusion: The

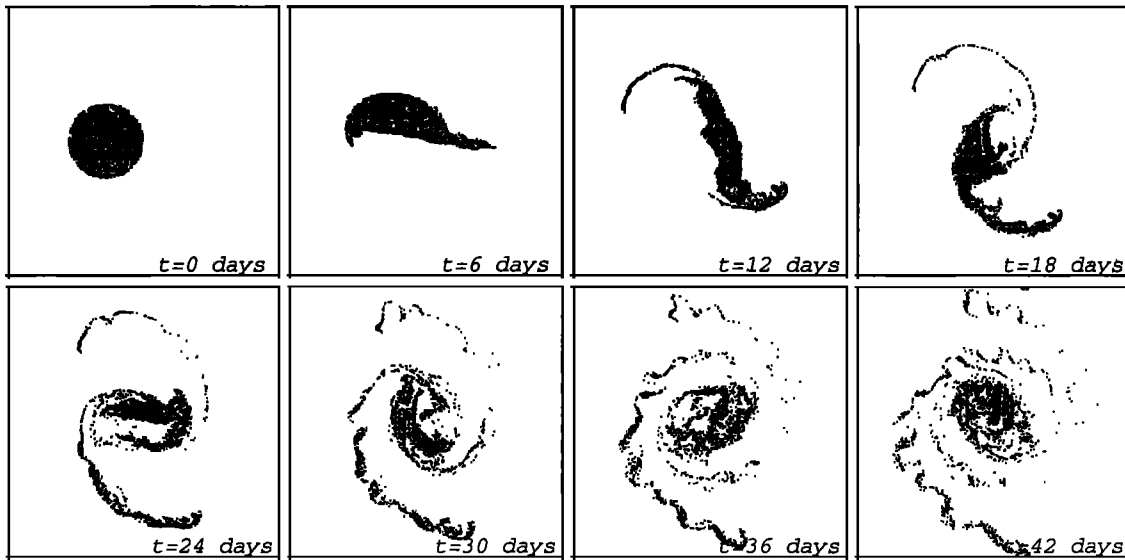


Figure 7. Same as for Figure 6a, but with the plots showing only the particles initially contained in the left vortex. Note the intrusion of this fluid around the other vortex during the early stages and the high degree of mixing in subsequent stages of the merging process. (If a traditional, Eulerian model had been used, the separation of fluid from each initial vortex would not have been an easy task.)

critical aspect ratio depends on the size of the vortex relatively to the deformation radius, but, for the common eddies in which the relative vorticity does not overcompensate the planetary vorticity, values lie slightly below 2.

These three studies, however, were performed with single-layer models. Since the ocean is stratified, we need to ask how the presence of baroclinicity affects the stability of an elliptical vortex. A logical start in that direction is the addition of a second moving layer, and the two-layer PIC model described above is appropriate for the task. One process requiring investigation is the feedback between layers: As an upper-layer elliptical lens vortex rotates, it perturbs the fluid thickness below thereby

causing, via potential-vorticity conservation, lower-layer vortical motions, which in turn affect the upper-layer vortex itself.

In this series of experiments, we choose an anticyclonic elongated eddy and perform a series of runs with varying eddy sizes, eccentricities, and lower-layer thicknesses. The eddy size is controlled by the parameter $\alpha = \sqrt{ab}/R_d$, where a and b are the semi-major and semi-minor axes, respectively, and R_d is the internal radius of deformation (based on the initial central depth of the upper layer: $R_d = \sqrt{g'H_1/f}$). The other control parameters are the initial aspect ratio $\gamma = a/b$ and the ratio of the thickness of the upper-layer and total depth $\delta = H_1/H$. We perform all our experiments on the f plane and

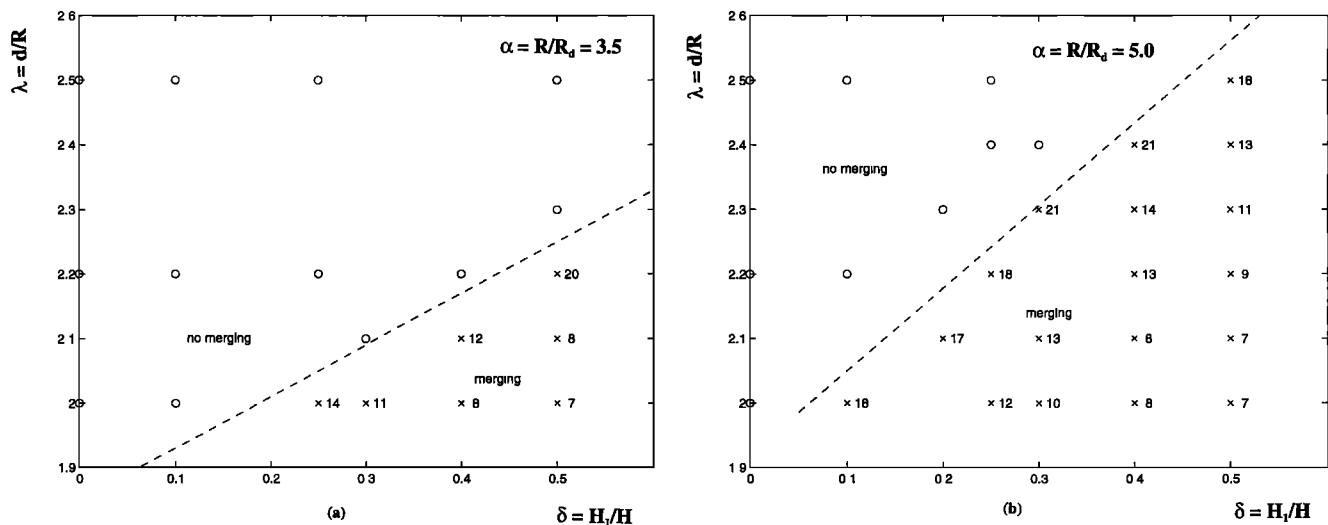


Figure 8. Recapitulation of merging experiments: (a) $\alpha = 3.5$ and (b) $\alpha = 5.0$. Numbers indicate the approximate duration (in days) of each merger event. An open circle indicates that merging did not occur for that particular combination of parameter values. Again, dimensionless time was converted using $f = 10^{-4} \text{ s}^{-1}$.

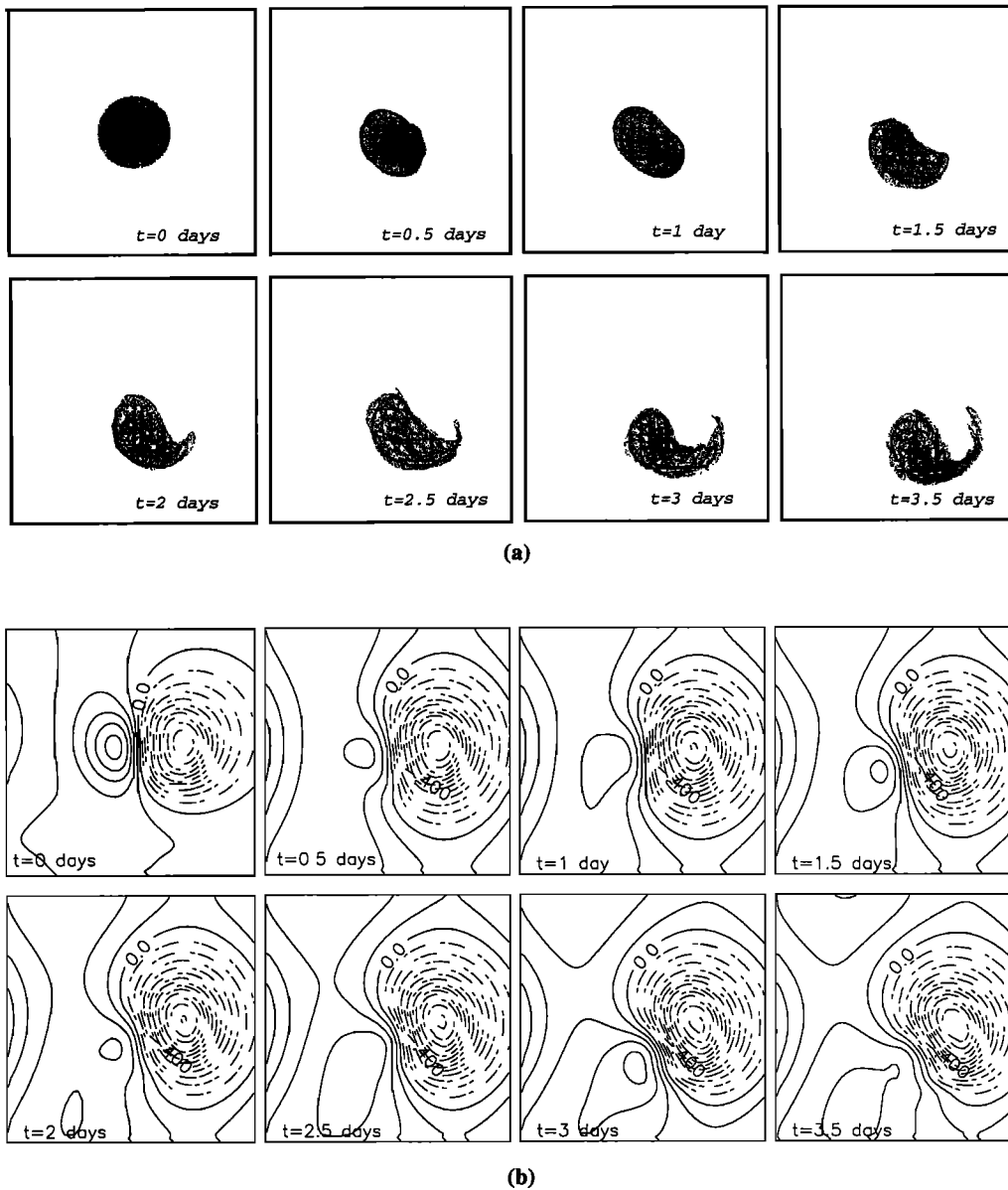


Figure 9. Evolution of a heton-type structure consisting of an upper-layer anticyclonic lens floating above, and slightly to the side of, a lower-layer cyclonic anomaly of opposite-sign potential vorticity: (a) upper-layer particles and (b) lower-layer pressure contours. Solid and dashed lines represent positive and negative values, respectively. Parameter values are $\alpha = R/R_d = 3.5$, $\lambda = d/R = 0.5$, and $\delta = H_1/H = 0.25$.

with zero lower-layer potential vorticity ($q_2 = 0$, although p_2 is not zero and varies in time).

Figures 2a and 2b show the behavior of a relatively large ($\alpha = 5.0$) and elongated ($\gamma = 3.0$) vortex over an active and finite lower layer ($\delta = 0.25$). We notice that filaments form at the vortex tips; these filaments become first elongated, then wind onto themselves, presumably as a result of lateral shear instability, and ultimately give rise to small vortices that surround the main vortex. The main vortex, remaining somewhat elongated, rotates and periodically collides with those smaller eddies, and repeated merging takes place. After about a full rotation of the central vortex, we note the presence of essentially three eddies: one central vortex of reduced eccentricity and two small circular eddies some distance away.

Figures 3a and 3b depict the evolution of a smaller initial

eddy ($\alpha = 3.5$) with the same initial eccentricity ($\gamma = 3.0$) and depth ratio ($\delta = 0.25$) as Figure 2. The eddy evolution in this case does not differ qualitatively from that of the one-layer case [Pavia and Cushman-Roisin, 1988], the only difference being the faster rate with which the eccentricity reduction occurs.

Comparing the evolution of the aspect ratio for a number of experiments (Figure 4), we note that all initially elongated vortices reduce their aspect ratio a/b to values in the range 1.75–1.85, which is not too different from the theoretical value of $\sqrt{7/2} = 1.871$. This comes somewhat as a surprise since the existing theory is valid only for large, reduced-gravity vortices (double limit $\alpha \rightarrow \infty$ and $\delta \rightarrow 0$). The theoretical stability criterion therefore appears to be a good predictor outside its range of applicability.

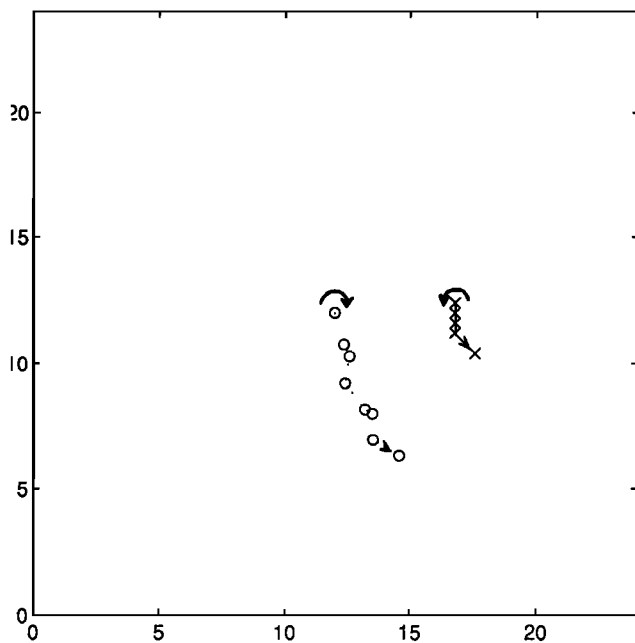


Figure 10. Trajectories of the upper-layer center of mass (circles) and of the lower-layer pressure minimum (crosses), in the heton-like structure of Figure 9. Marks along the trajectories indicate half-day intervals; the duration of the simulation is 3.5 days. Note how the vortex centers move as a pair along nearly concentric circular arcs.

To test further the relevance of the large-size, reduced-gravity stability theory to the finite-size, two-layer case, we performed an additional run with a vortex of initial aspect ratio $\gamma = 1.6$, which lies below the theoretical threshold value. Except for leaving a very thin trail of particles as it rotates, the eddy retained its shape after two full rotations.

Another observation stemming from our experiments is that smaller vortices rotate faster than the larger ones (Figure 5). The one-layer model [Cushman-Roisin *et al.*, 1985] predicts eddy rotation rates decreasing like the negative fourth power of the eddy radius. While this relation is borne in the $\delta = 0$ limit, simulations with finite lower-layer depths reveal a less precipitous drop in rotation rate with increasing size. In addition, we note that the initial rotation rate of the vortex increases almost linearly with δ , i.e., the thinner the lower layer, the faster the vortex rotation. This is in complete agreement with the theoretical findings of Cushman-Roisin and Merchant-Both [1995].

Other factors may influence the rotation rate of the vortex besides its size and the layer-thickness ratio. For example, an imbalance between centrifugal, Coriolis, and pressure forces in the initial state causes a pulsation of the eddy which, in turn, may affect its rotation rate. Another possible agent is friction. The study of these additional processes is left for further studies.

3.3. Horizontal Interaction of Two Circular Vortices

In a second series of experiments, we explore the horizontal interaction of two frontal vortices, which may or may not include a merger of the two vortex cores. We do so by initializing the model with two identical circular anticyclonic lenses placed some distance apart. This problem is pertinent since numerical simulations of quasi-two-dimensional turbulent flows [e.g.,

McWilliams, 1984; Cushman-Roisin and Tang, 1990] indicate that eddy merging is a spontaneous process, driving the so-called reverse cascade of energy toward large scales. This gives us a good reason to believe that eddy merging occurs in the ocean. And, indeed, there are reports of such encounters, although these are few, presumably more because of logistical difficulties than because of the rarity of this type of event. Two noteworthy reports are those of Creswell [1982] documenting the merger of two anticyclonic eddies in the vicinity of the East Australian Current and of Yasuda *et al.* [1992] tracing the interaction of two Kuroshio rings. In addition, the coalescence of Aghulas Current rings has been inferred from satellite imagery [van Ballegooyen, 1994], and there are strong reasons to believe that Mediterranean salt lenses, also, may occasionally merge [Schultz-Tokos *et al.*, 1994].

The two-vortex problem has been the object of much attention. Our present purpose is not to offer an extensive review but only to situate our numerical experiments in the context of previous investigations. Almost all previous numerical studies have been conducted with quasi-geostrophic models, discretized by either finite differences [e.g., Melander *et al.*, 1988; Valcke and Verron, 1997; Yasuda and Flierl, 1997] or contour dynamics [e.g., Polvani *et al.*, 1989]. Although these investigations have been conducted with much attention paid to accuracy, it nonetheless remains that they are fundamentally restricted by the underlying quasi-geostrophic assumption of small vertical displacements, and it is unclear whether, or to which extent, the results can be extrapolated to frontal vortices, with outcropping interface.

The particular study of the merging of lens-like vortices (with outcropping interface) begun with a theoretical argument indicating that spontaneous coalescence of such vortices was energetically prohibited [Gill and Griffiths, 1981]. This conclusion is contradicted by the observational evidence [Gill and Griffiths, 1981] as well as laboratory evidence [Griffiths and Hopfinger, 1987]. The paradox was resolved by Cushman-Roisin [1989], who noted that the rejection of core fluid by the process of filamentation yields a final state that consists in more than a single, compound vortex. When account is made for the volume, angular momentum, and energy contained in the surrounding filaments, the merger event is no longer found energetically prohibited. However, this theoretical study only considered initial and final states, leaving undocumented the actual evolutionary pathway.

To date, the only existing numerical study detailing the process of merging of two lens-like anticyclones is that of Pavia and Cushman-Roisin [1990]. This study was based on an earlier, one-layer version of the present PIC model and confirmed the spontaneous character of frontal-vortex merger and the crucial role played by filamentation during the process. We now extend this study to include the influence of an active second lower layer. In particular, we investigate how the minimum distance between initial vortices required for merging depends on the layer-depth ratio (a crude measure of the ambient stratification). In essence, this extends the recent study by Valcke and Verron [1997] on the effect of a second layer on quasi-geostrophic vortex merger to frontal vortices.

We initialize our f plane, two-layer model by constructing two identical circular vortices of central depth H_1 and radius R , separated by a center-to-center distance d ($d \geq 2R$, to avoid overlap). The independent dimensionless parameters are $\alpha = R/R_d$ (where $R_d = \sqrt{g'H_1/f}$), $\lambda = d/R$, and $\delta = H_1/H$,

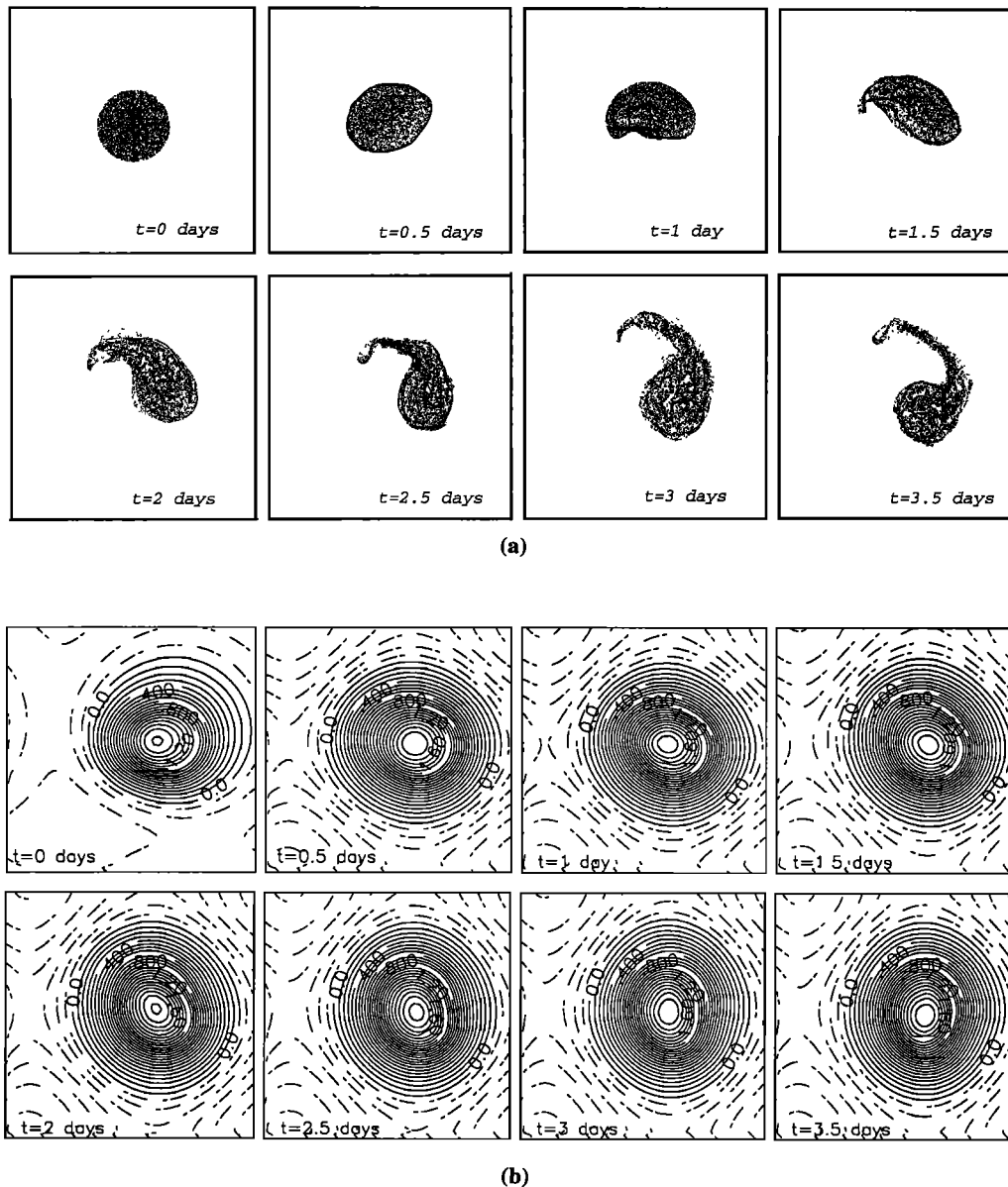


Figure 11. Evolution of a vortex structure consisting of an upper-layer anticyclonic lens floating above, and slightly to the side of, a lower-layer anticyclonic anomaly of same-sign potential vorticity: (a) upper-layer particles and (b) lower-layer pressure contours. Solid and dashed lines represent positive and negative values, respectively. Parameter values are $\alpha = R/R_d = 3.5$, $\lambda = d/R = 0.5$, and $\delta = H_1/H = 0.25$.

which measure respectively the eddy size, the separation distance, and the importance of the lower layer. The lower-layer potential vorticity is again set to a uniform zero value.

In contrast to the one-layer model [Pavia and Cushman-Roisin, 1990], where the lack of eddy interaction outside of each outcrop prevented merging unless there was an initial overlap, our present simulations with two active layers indicate that vortex lenses can merge with nonzero separation distance. The explanation lies in the lower-layer pressure field, which extends well beyond the eddy rim, allowing the vortices to feel each other's remote presence. Merging therefore occurs without initial overlap, although the tendency to merge obviously decreases with initial separation between eddies.

Figures 6a and 6b depict the evolution of the particle's positions and of the upper-layer thickness in the case of $\delta =$

0.25, with each eddy radius being 5 times the radius of deformation ($\alpha = 5.0$) and initially touching ($\lambda = 2$). The first stage in the merging process involves the wrapping of the eddies around each other (Figure 7). Then, while the new aggregate eddy structure is in this transient state, its elongation causes it to rotate, and filaments begin to form at the extremities. The next stage is the merging itself, during which an elongated eddy with a single center (depth maximum) is formed, while further filamentation occurs at the two vortex tips. In the final stage, the elongated eddy partially axisymmetrizes, and the filaments roll up to form a constellation of smaller satellite eddies. We also observe that the depth of the final eddy is almost the same as that of the initial eddies and that its radius is not much larger than theirs. This leads us to conclude that the merged eddy is only slightly larger in volume than each of the initial

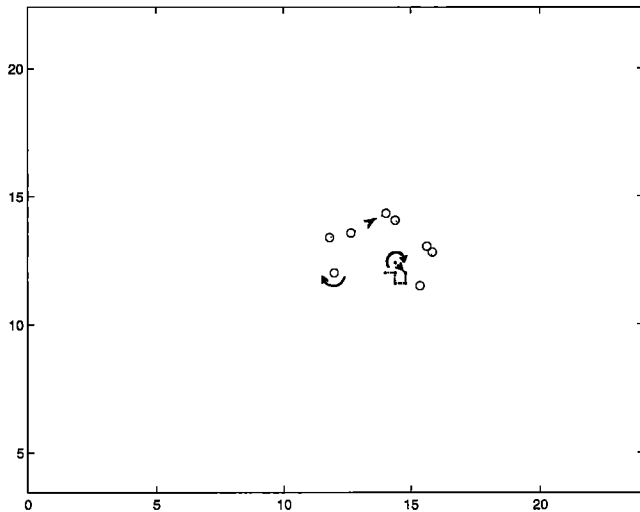


Figure 12. Trajectories of the upper-layer center of mass (circles) and of the lower-layer pressure minimum (crosses), in the vortex structure of Figure 11. Marks along the trajectories indicate half-day intervals; the duration of the simulation is 3.5 days. Note how the vortex centers rotate counterclockwise, as if chasing each other. There is also a tendency toward vertical alignment.

eddies. Calculations show that $\sim 40\%$ of the total volume is taken by the filaments.

Experiments with other parameter values exhibit either qualitatively similar features or the absence of merging. Collectively, they conclusively demonstrate that an active lower layer exerts a profound influence upon the merging of the vortices. For example, medium-size vortices ($\alpha = 3.5$) merge if they are grazing ($\lambda = 2.0$) for δ values of 0.5 and 0.25. When the distance between the same eddies is increased by 10% ($\lambda = 2.2$), merging no longer takes place for $\delta = 0.25$ but still takes place for $\delta = 0.5$. For larger vortices ($\alpha = 5.0$), merging from a grazing condition takes place for δ values of 0.1, 0.25, and 0.5. However, for an infinitely deep lower layer ($\delta = 0$), there is no merging, in agreement with the earlier results of *Pavia and Cushman-Roisin* [1990]. Put another way, there exists a minimum separation distance for merging, which depends on both vortex size and layer-depth ratio. Figure 8 recapitulates our simulations and clearly shows how the critical separation distance necessary for merging depends on the depth ratio δ for two distinct vortex sizes ($\alpha = 3.5$ and 5.0). From our set of experiments, we empirically derive that merging occurs if $\lambda < 1.73 + 0.32(\alpha - 1.0)(\delta + 0.15)$, although this criterion is imprecise because it is very difficult to distinguish in numerical experiments between a very long merger and the absence of merging. We also note that the merging time (time until stabilization of the central vortex) is nearly inversely proportional to the depth ratio δ and directly proportional to the distance ratio λ . Vortices that are too far apart to merge exhibit a simple mutual rotation, as we can anticipate by extrapolation of point-vortex studies [*Aref*, 1983, and references therein].

3.4. Vertical Interaction of Vortices

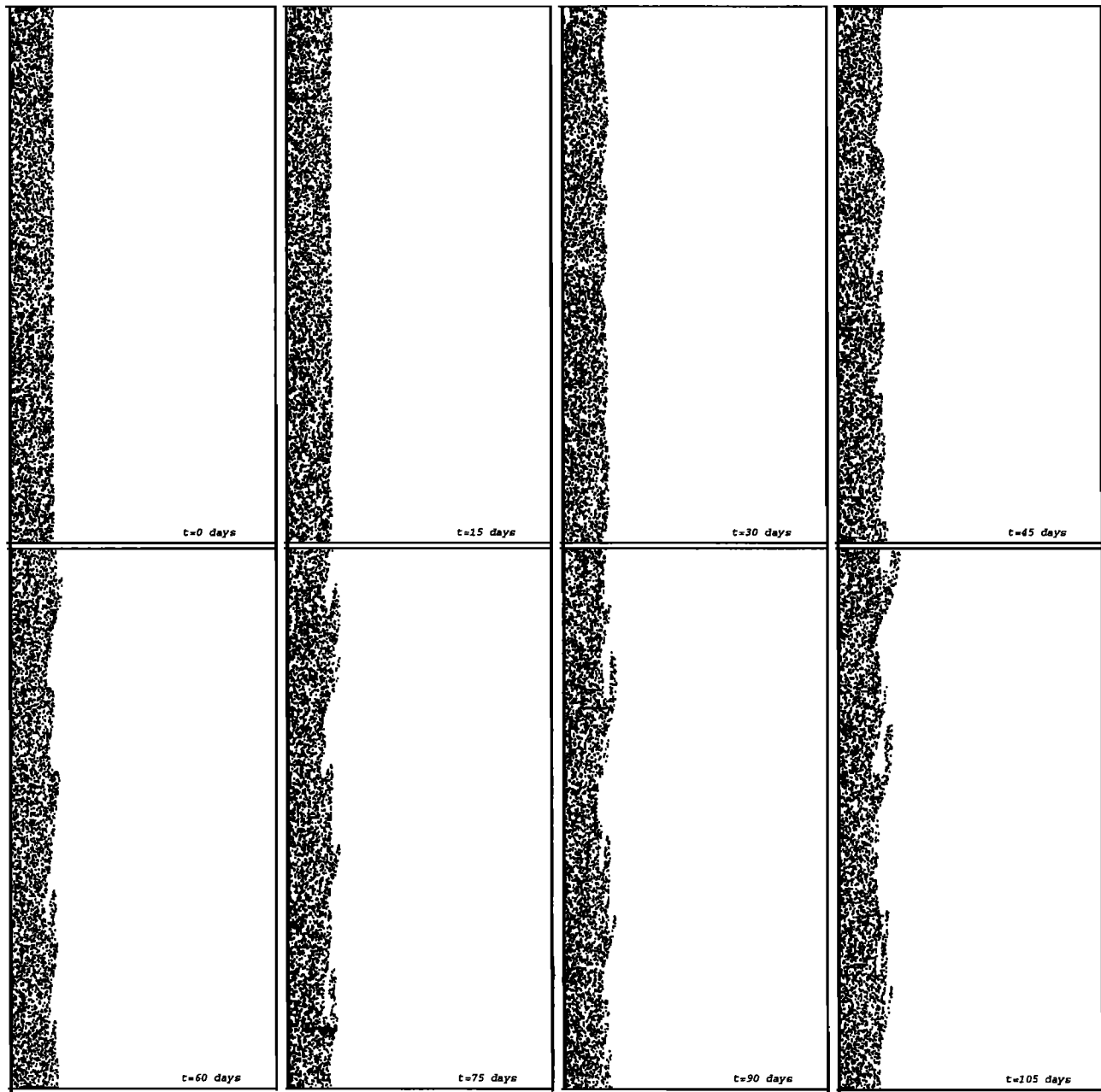
In a two-layer system, distinct vortices do not have to lie in the same layer, and we may ask how a vortex in one layer interacts with a nearby vortex in the other layer. *Hogg and Stommel* [1985] were the first to address this question by study-

ing the behavior of point vortices in a two-layer quasi-geostrophic system, paying particular attention to pairs consisting of opposite-signed vortices, which they called "hetons." Soon afterward *Griffiths and Hopfinger* [1986] carried out laboratory experiments designed to verify the theoretical predictions of *Hogg and Stommel* [1985]. They thus ensured that the vertical deflections induced by the vortices at the density interface were sufficiently weak to satisfy the quasi-geostrophic approximation. Despite the fact that laboratory vortices necessarily have finite areas (particularly the anticyclones, which are formed by fluid injection), the behaviors of laboratory and point-vortex hetons were found to be in substantial agreement. As a rule, hetons self-propagate as pairs, following a straight path if the two components have equal strength, and a curved path, otherwise. Complicated interactions, which may include re-pairing, occur when two hetons collide.

Later, *Polvani* [1991] performed simulations with the contour-dynamics method, in essence extending the study of *Hogg and Stommel* [1985] from point to finite-area vortices. Besides verifying the overall behavior of point hetons when the two vortices have opposite polarities, *Polvani* [1991] also studied the behavior of like-signed vortices (two identical vortices but one in each layer, a small horizontal distance apart from each other) and discovered a tendency toward vertical alignment. In some ways, such alignment is the counterpart of coalescence when the vortices lie in distinct layers. Because the method of contour dynamics crucially depends on the assumption of quasi-geostrophy, vertical displacements of the density interface were again in this study necessarily very small.

On the contrary, the PIC method allows finite vertical displacements, even outcropping, of the density interface. We are therefore in a position to extend the investigation of hetons to cases when the upper-layer vortex has a frontal character. From the perspective of our PIC method, the most natural structure of a heton-like formation is an upper-layer anticyclonic lens floating above, and slightly to the side of, a lower-layer circular patch of cyclonic potential vorticity. To minimize the number of parameters, we assign the same radius R to both upper-layer lens and lower-layer anomaly and set the potential-vorticity anomaly at a uniform value: $q_2 = +fH_1/H$. (In the present context, it is not possible to maintain quasi-geostrophy in the lower layer and simultaneously enforce total compensation of anticyclonic and cyclonic vorticities in the overall structure. The upper-layer potential vorticity varies radially, reaching infinity at the outcrop.) With the definition of the deformation radius R_d again based on the initial center depth H_1 of the lens, the dimensionless parameters are $\alpha = R/R_d$, measuring the size of the vortices; $\lambda = d/R$, measuring the separation distance d between the vortex centers; and $\delta = H_1/H$, measuring the importance of the coupling between the layers.

Figures 9a and 9b show the evolution of the upper-layer particles and lower-layer pressure field when the parameter values are $\alpha = 3.5$, $\lambda = 0.5$, and $\delta = 0.25$. From the sequence of plots, it is evident that the two vortices distort somewhat to adjust to each other's presence but retain their integrity and that they entrain each other in their respective sense of rotation. If we track the two vortex centers by locating the center of mass of the upper-layer particles and the point of minimum pressure in the lower layer, we obtain Figure 10, which shows more clearly the mutual advection of the vortex pair. The trajectories appear as concentric circular arcs. These results extend beyond the quasi-geostrophic approximation of the



(a)

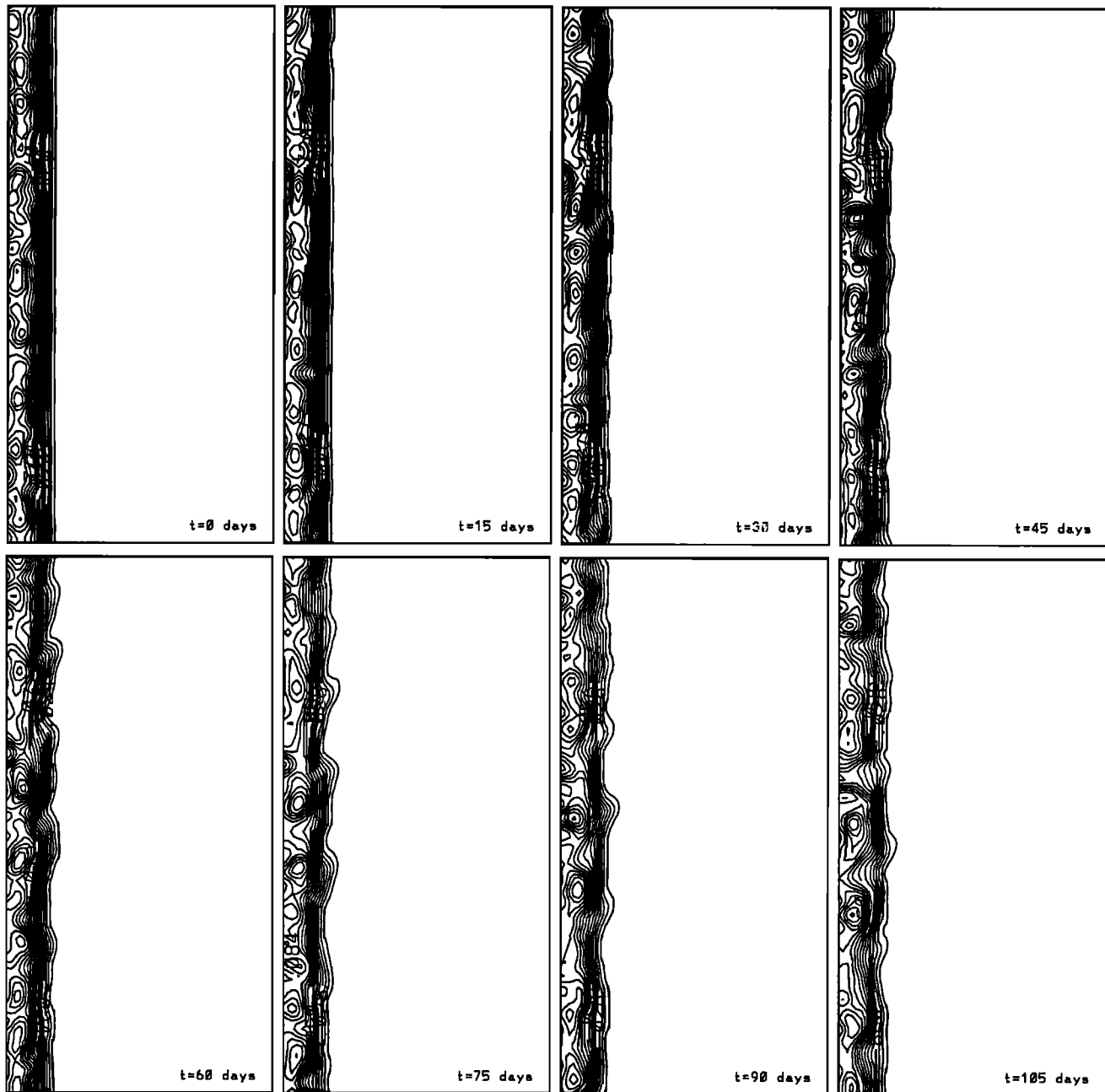
Figure 13. (a) Particle positions and (b) corresponding upper-layer thickness contours during the evolution of a coastal current with offshore front. The coast is on the left side and the general flow is down the page. Parameter values are $Bu = 2.8 \times 10^{-3}$ and $\delta = 0.1$.

findings of *Hogg and Stommel* [1985] and of *Griffiths and Hopfinger* [1986], who found that quasi-geostrophic hetons translate (or corotate with the center of corotation lying outside the trajectories of the individual vortex centers).

Additional simulations with different parameter values indicate that the radii of the vortex-center trajectories increase with increasing initial separation. A greater initial separation also gives rise to a slower drift of the two-vortex structure. Increasing the thickness of the bottom layer decreases the drift speed but does not appear to affect significantly the radii of the trajectories.

In a separate series of experiments, we set the lower-layer

potential-vorticity anomaly to a negative value ($q_2 = -fH_1/H$), yielding a compound system with two vorticities of the same (anticyclonic) polarity, one in each layer. According to *Polvani* [1991], the quasi-geostrophic version of this situation leads to mutual rotation with a tendency toward vertical alignment. As for the previous series of experiments, our simulations reveal a similar evolution (Figure 11). The upper-layer lens executes a clockwise rotation around the lower-layer vortex. Less evident but nonetheless present is the clockwise trajectory of shorter radius traced by the latter (Figure 12). Thus both vortices rotate around each other. Also noticeable on Figure 12 is the gradual reduction of the distance separating



(b)

Figure 13. (continued)

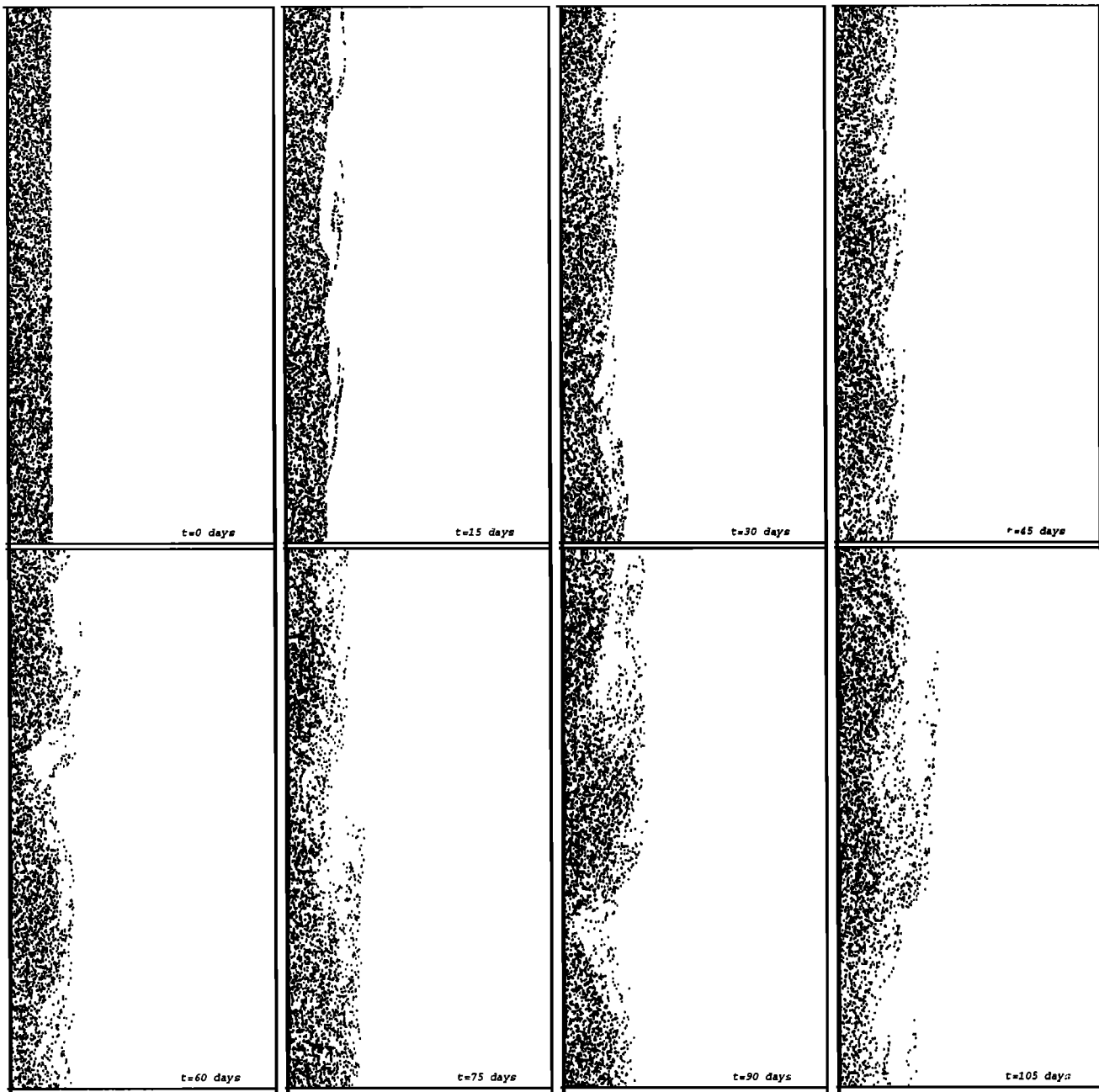
the two vortex centers. This tendency toward vertical alignment extends the finding of *Polvani* [1991] beyond the quasi-geostrophic approximation to situations with finite vertical displacements of the density interface.

Additional simulations provide the following parametric variations. When the upper-layer thickness is a quarter of the total depth of the two-layer system ($\delta = 0.25$), the radius of the path of the upper vortex increases with the initial horizontal separation of the vortices. The trajectories nearly coincide (although the 180° phase shift remains) when the distance between the centers are equal to the radius of each vortex, i.e., when each vortex moves along the rim of the other. When the

upper-layer thickness is one tenth of the total depth of the two-layer system ($\delta = 0.1$), the radius of the path of the lens center is always shorter than that of the path of the lower vortex. Finally, the relative velocity of the vortex centers decreases with increasing lower-layer thickness and with increasing vortex separation.

4. Coastal Buoyancy Current Simulations

Coastal buoyancy currents are quite common in the oceans. Most occur because horizontal density differences (associated with coastal processes) and Coriolis effects combine to pro-



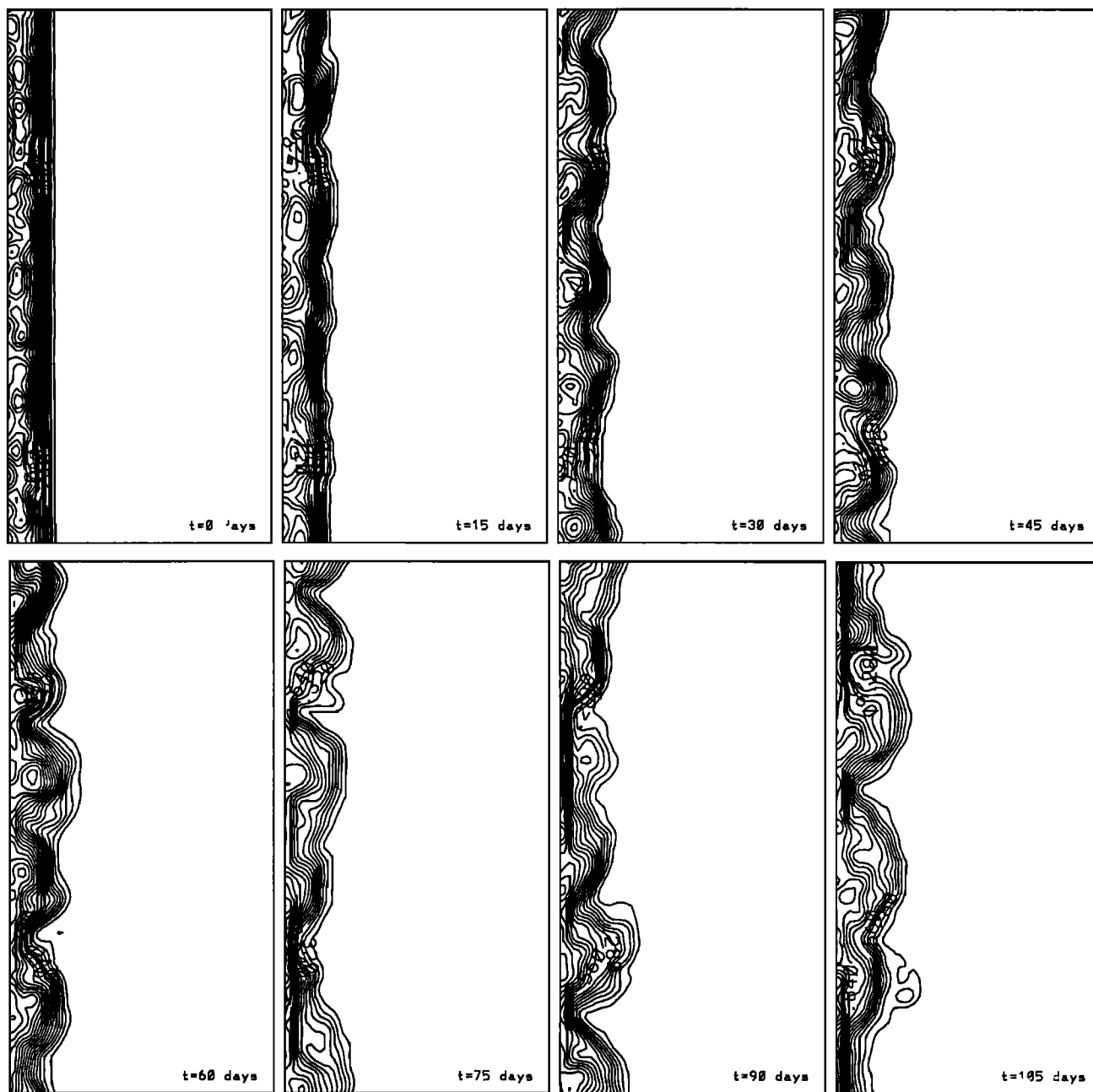
(a)

Figure 14. Same as Figure 13, but for $Bu = 2.8 \times 10^{-2}$ and $\delta = 0.1$.

duce geostrophic currents parallel to the coast, flowing with the coast on the right in Northern Hemisphere. Despite their relative spatial confinement and temporal persistence, all coastal buoyancy currents exhibit a considerable degree of wave-like behavior and instability [Mork, 1981; McClimans and Nilsen, 1982; Royer, 1982; Millot, 1985; Griffiths and Pearce, 1985; Kowalik *et al.*, 1994]. What is known about the dynamics of this variability in the case of a current bounded offshore by a front has been provided by theoretical studies based on severely limiting assumptions, such as infinitesimally small perturbations or very long wavelengths [Killworth and Stern, 1982; Paldor, 1983, 1988] and by laboratory simulations [Griffiths and Linden, 1981, 1982; McClimans *et al.*, 1985].

Our present interest is in discerning the possible outcomes under varying parameters (current width, frontal strength, etc.). Because we are not interested in the behavior of the nose of a progressing coastal intrusion (which this model is able to simulate, but which we defer to a further study), we shall assume that the coastal current preexists and occupies the entire length of the coastline and moreover that it is initially in steady geostrophic balance.

For our experiments with a coastal boundary, we choose a rectangular channel bounded by vertical walls at $x = 0$ and $x = D$ (where D is the channel width) and open on the two remaining sides. Along these open boundaries, we impose periodic boundary conditions, while along the x boundaries, we



(b)

Figure 14. (continued)

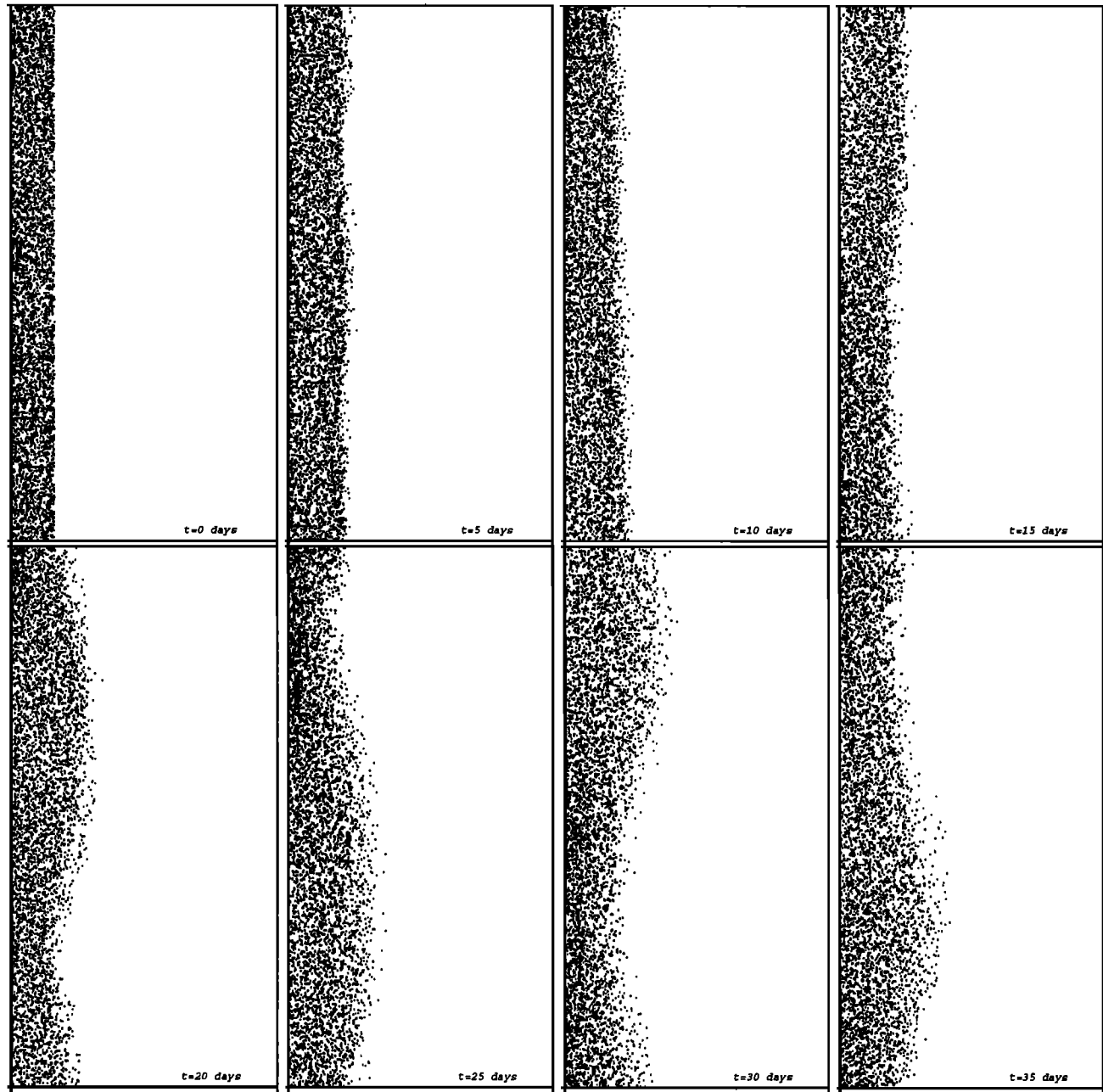
impose no normal flow ($u = 0$ at $x = 0, D$). In the PIC method, this is accomplished by a momentum-conserving reflection scheme [Sanson *et al.*, 1998; Cushman-Roisin *et al.*, 1999]: A particle that would be moved beyond a wall (say $x = 0$) is instead reflected into the domain ($x_k^{new} = -x_k^{old}$ and $y_k^{new} = y_k^{old}$, where new refers to the state immediately following the reflection and old refers to that preceding it) with conserved total momentum in the tangential direction [$v_k^{new} = v_k^{old} + f(x_k^{old} - x_k^{new})$] and opposite normal velocity ($u_k^{new} = -\sigma u_k^{old}$, where the factor σ is set to enforce conservation of kinetic energy, $(u_k^{new})^2 + (v_k^{new})^2 = (u_k^{old})^2 + (v_k^{old})^2$). In the lower layer, geostrophy implies $\partial p_2 / \partial y = 0$; that is, $p_2 = \text{constant}$ at $x = 0, D$.

We use a 60×120 grid and $N = 12,000$ particles. To initialize the system, particles are first randomly and uniformly distributed over an area $a \times b$, where a is the width of the current and b the length of the domain in the y direction, according to

$$x_k = an_1 \quad y_k = bn_2 \tag{17}$$

where (n_1, n_2) is the k th pair in a series of random numbers between 0 and 1. For all our runs, we take $b = 12a$ to allow a sufficient number of waves along the current and thereby reduce the effect of quantization (integer number of waves between periodic boundaries).

Because of their random positioning, all particles share the



(a)

Figure 15. Same as Figure 13, but for $Bu = 0.28$ and $\delta = 0.1$.

same cross-sectional area, equal to ab/N . Then each particle is assigned a volume depending on its actual position in the current and the prescribed profile of the latter. In all our simulations, we use a parabolic profile, $h_1(x) = H_1(1 - x^2/a^2)$, which has a maximum thickness at the coast ($h_1 = H_1$ at $x = 0$) and a front offshore ($h_1 = 0$ at $x = a$). So, the volume V_k of particle k is

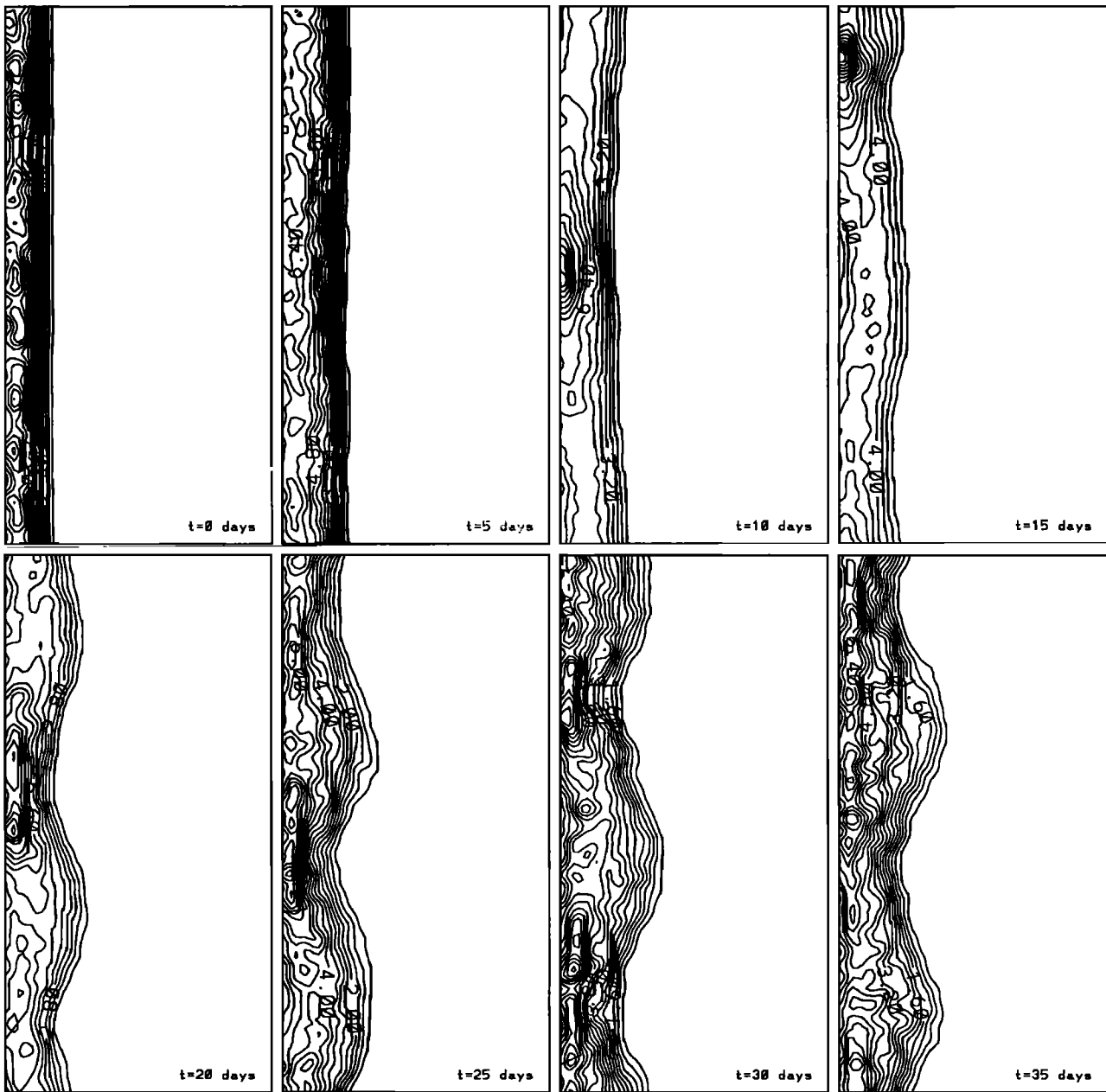
$$V_k = H_1 \left(1 - \frac{x_k^2}{a^2} \right) \frac{ab}{N} \tag{18}$$

We then assign initial velocity components to every particle by requiring that the current be initially in geostrophic equilibrium:

$$u_k = 0 \quad v_k = \frac{1}{\rho_0 f} \left. \frac{\partial p_1}{\partial x} \right|_k \tag{19}$$

However, because $p_1 = p_2 + \rho_0 g' h_1$, we first need to calculate the initial pressure distribution in the lower layer, using (10). Taking a uniform potential vorticity in the lower layer [$q_2(t = 0) = 0$], we need to solve $\nabla^2 p_2 = -(\rho_0 f^2/H)h_1$, with the boundary conditions $p_2 = 0$ and $\partial p_2/\partial x = 0$ at $x = a$ (for match with the stagnant lower layer offshore of the front) and periodicity in y . The solution is

$$p_2 = \frac{\rho_0 f^2 H_1}{H} \left(\frac{x^4}{12a^2} - \frac{x^2}{2} + \frac{2ax}{3} - \frac{a^2}{4} \right) \tag{20}$$



(b)

Figure 15. (continued)

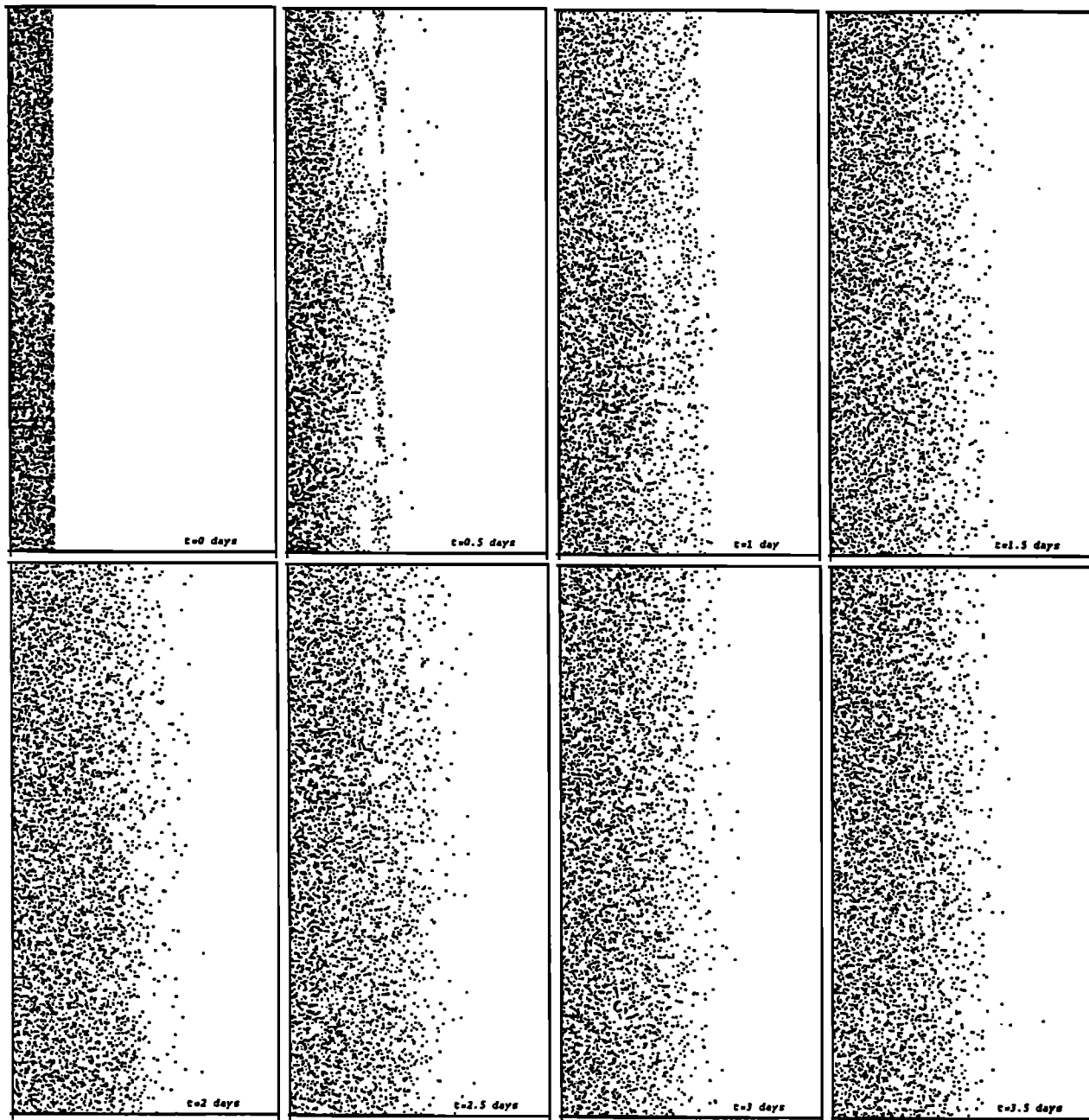
from which we finally derive the alongshore particle velocities:

$$v_k = -\frac{2g'H_1x_k}{fa^2} + \frac{faH_1}{H} \left(\frac{x_k^3}{3a^3} - \frac{x_k}{a} + \frac{2}{3} \right) \quad (21)$$

Note that this velocity does not vanish at the coast, although its residual value there is entirely due to a lower-layer effect, which vanishes in the limit of a very deep ocean ($H_1/H \rightarrow 0$).

Coastal currents in our numerical experiments can be characterized by their geometric structure, i.e., initial width a , buoyancy g' , and coastal depth H_1 . The nondimensional number that combines these characteristics is the so-called Burger number, $Bu = g'H_1/f^2a^2$ (or equivalently, a rotational densimetric Froude number [McClimans *et al.*, 1985]). Every ex-

periment can then be characterized by two dimensionless numbers, the Burger number (Bu) and the vertical aspect ratio ($\delta = H_1/H$). The former is an estimate of the ratio of kinetic to available potential energy of the flow, while the latter measures the importance of the lower layer. Together these parameters permit to distinguish among different regimes of instabilities. Because oceanic observations reveal that the majority of coastal buoyancy currents falls in those ranges of parameter values, we perform our experiments with $10^{-4} < Bu < 0.5$ and $0.1 < \delta < 0.25$. ($Bu = 0.5$ is actually an upper bound for this type of flow, as shown in the appendix.) In our runs, we vary the Burger number by changing the coastal depth H_1 and keeping the width a constant.



(a)

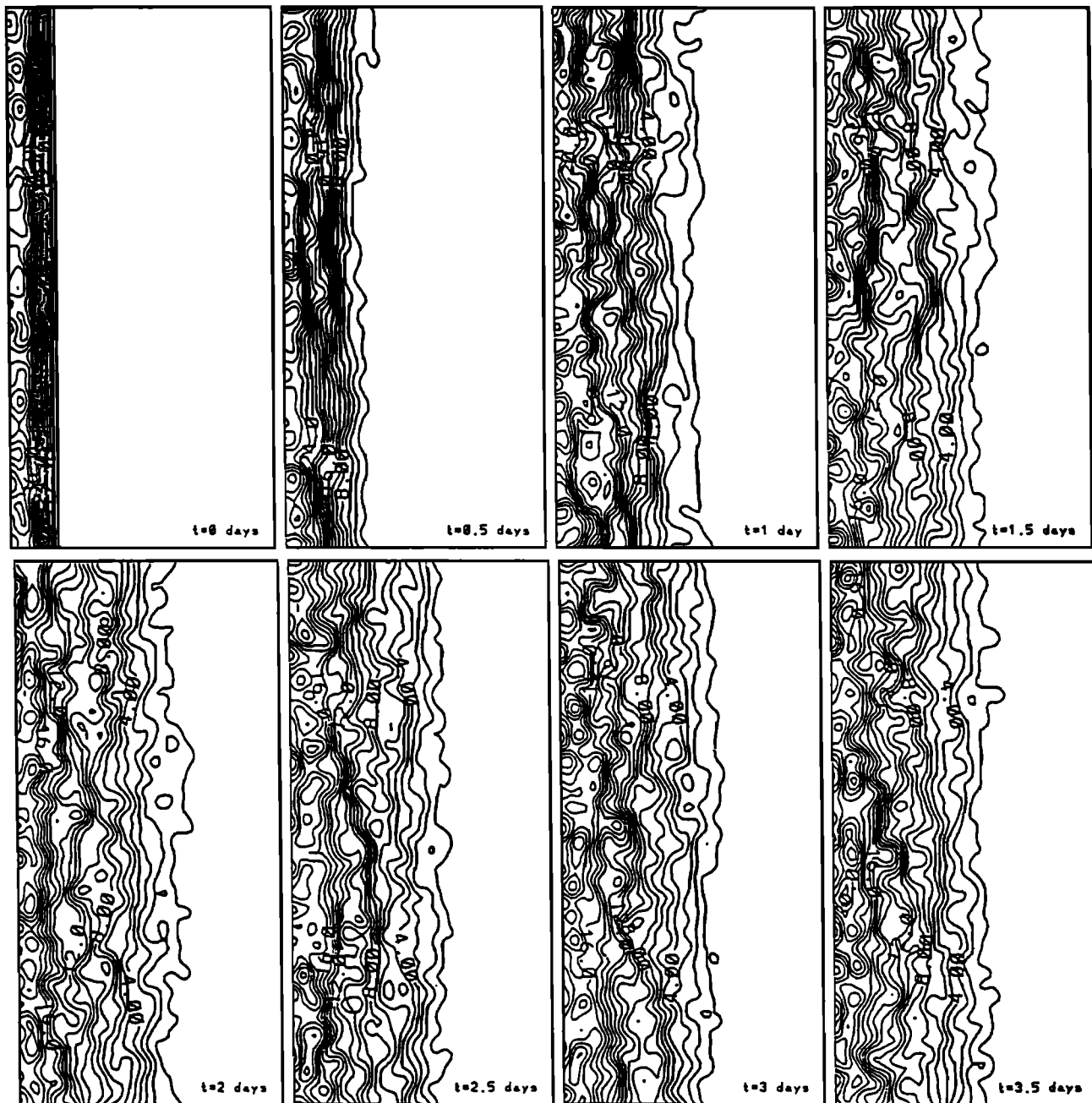
Figure 16. Same as Figure 13, but for $Bu = 1.4$ and $\delta = 0.1$.

We start with a small Burger number ($Bu = 2.8 \times 10^{-4}$) and aspect ratio ($\delta = 0.1$), corresponding to a very broad current over a relatively deep lower layer. The flow is found to be stable, preserving its shape for the entire duration of the simulation (144 inertial periods). The existing horizontal shear is apparently too weak to cause a barotropic instability, while the large width of the current implies a weakly sloping interface, which, in conjunction with a deep lower layer, most likely precludes baroclinic instability.

When we increase the Burger number by a factor of 10 ($Bu = 2.8 \times 10^{-3}$), we note that finite-amplitude perturbations emerge and propagate downstream (Figure 13). These wave-like structures have a characteristic wavelength compa-

table to the radius of deformation but have weak amplitudes (they are squeezed in the offshore direction). Another interesting feature is the formation of vortices embedded in the mean current (Figure 13b). The fact that these structures have a characteristic length scale of the order of the radius of deformation is an indication that baroclinic instability may play an important role in the evolution of the current.

A further increase of the Burger number ($Bu = 2.8 \times 10^{-2}$), which corresponds to a deeper and/or narrower current, reveals a more interesting behavior (Figure 14). In this case, the essence of the instability is probably a mixed barotropic-baroclinic instability (barotropic because of the large velocity shear at the front and baroclinic because the initial



(b)

Figure 16. (continued)

current width is of the order of the deformation radius based on the initial coastal thickness). The distortion of the frontline is not only faster but also larger than in the cases with smaller Burger numbers. The instability is manifested by severe localized pinching of the current and vigorous backward wave breaking, which lead to intense stirring across the flow. A coastal current with a still higher Burger number ($Bu = 0.28$), approaching the dynamical limit of 0.50 (see appendix), develops perturbations of even longer wavelengths but causing less pinching of the current (Figure 15).

Figure 16 demonstrates that for $Bu = 1.4$, a value exceeding the dynamical limit, the current is inertially unstable with no dominant wavelength and the emerging picture is that of a

well-developed geostrophic turbulence between coast and front. (After a few days, the numerical accuracy for this run has fallen sharply as the width of the current has increased and the number of particles per cell has dropped to an unacceptably low level. A more precise run would require a much larger number of particles. This we did not do because it is enough to know that such coastal current is very short lived and could not exist in the real ocean.)

Simulations with a shallower and therefore more active lower layer ($\delta = 0.2$) show that the larger the Burger number the bigger the differences with the previous cases ($\delta = 0.1$). Indeed, on the f plane, the squeezing or stretching of fluid columns in the lower layer can be compensated only by mod-

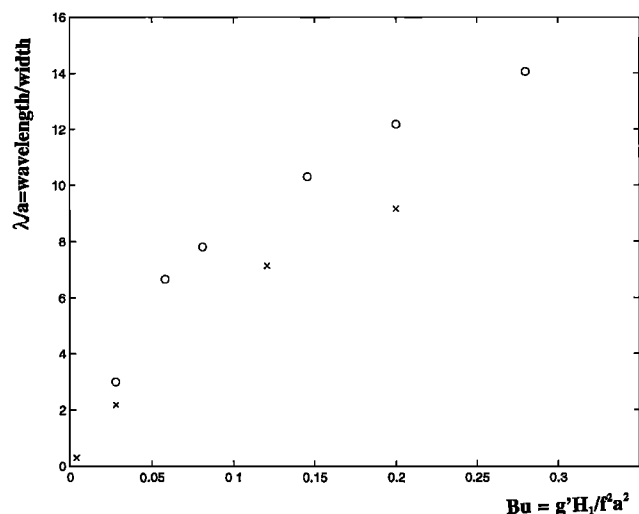


Figure 17. Dependence of the wavelength of the most unstable disturbance along a coastal front on the Burger number of the associated current. Circles and crosses correspond, respectively, to a deeper and shallower lower layer ($\delta = 0.1$ and $\delta = 0.2$).

ifications in relative vorticity. A greater depth ratio, which implies greater relative stretching and squeezing of the lower layer under the action of upper-layer motions therefore creates stronger flows in the lower layer and a greater feedback on the upper layer. The dependency of the most unstable wavelength on the Burger number Bu and the depth ratio δ is shown in Figure 17. The result is that the ratio λ/a of the wavelength λ to the current width a increases with the Burger number as $Bu^{1/2}$ and decreases with the depth ratio δ , in accordance with the laboratory findings of *Griffiths and Linden* [1982] and with the observations of the meandering of the Norwegian Coastal Current reported by *McClimans et al.* [1985]. The proportionality between λ/a and $Bu^{1/2}$ is clear in our simulations, but the dependency of λ/a on δ is more difficult to establish, for it does not clearly follow a power law; a rough fit yields proportionality to δ^{-n} with $n = 0.5 \pm 0.1$, significantly different from $n = 0.25$ found by *Griffiths and Linden* [1982]. This matter demands additional investigation.

5. Conclusions

We applied an augmented, two-layer version of a particle-in-cell (PIC) method to problems in mesoscale oceanography in which the interface separating two layers of constant density intersects the surface along one or several fronts that distort over time. While the use of a more traditional numerical method would have demanded that we overcome a number of computational issues, we demonstrated that the PIC method is very versatile and capable of deriving a number of useful results in a broad range of problems.

In a first series of simulations, the flow field was initialized with a single anticyclonic lens vortex of elliptical shape. Nearly all vortices exhibited a clear tendency toward eccentricity reduction but resisted complete axisymmetrization. Their final aspect ratio (semimajor axis over semiminor axis, a/b) was found to lie in the rather limited range $1.75 < a/b < 1.85$, almost independently of their initial aspect ratio and of the lower-layer depth. Furthermore, these values are not far from

the theoretical stability threshold found for large, reduced-gravity lenses ($a/b = 1.871$). Invariably, the evolution proceeded with an anticyclonic rotation of the vortex during which filaments were shed in the wake of its two tips. These filaments in turn exhibited instabilities, breaking into segments that rolled into small eddies. The only vortices that showed no tendency toward eccentricity reduction were those whose aspect ratio lay below 1.75 initially.

Next, we revisited the classical problem of vortex merging, this time with two anticyclonic lens-like vortices atop of a lower layer finite depth. While the two upper-layer vortices were placed apart from each other, and thus by virtue of their frontal character did not overlap at all in that layer, the pressure distributions they induced in the lower layer created nonetheless an interaction, which led either to merging into a new, larger vortex or to mutual rotation. Merging occurred if the initial separation distance d between vortex centers did not exceed a certain value depending upon their initial radius R , center depth H_1 , and depth of the lower layer H , namely $d/R < 1.73 + 0.32(fR/\sqrt{g'H_1} - 1.0)(H_1/H + 0.15)$. In every merging situation, once the new vortex core was formed, a certain elongation was present, which then led to anticyclonic rotation, filamentation, and partial eccentricity reduction.

In a third series of simulations, the flow field was initialized with one circular anticyclonic vortex in the upper layer above, and slightly to the side of, a potential-vorticity anomaly in the lower layer. When this anomaly corresponded to a cyclonic vorticity (i.e., the heton configuration of point vortices), results very similar to those obtained with quasi-geostrophic point vortices and contour dynamics (co-induced translation along a circular path) were noted, thereby extending known results to the non-quasi-geostrophic dynamical regime. When the lower-layer potential-vorticity anomaly corresponded to anticyclonic vorticity, we noted a mutually induced corotation of the vortex centers accompanied by a tendency toward vertical alignment. This result, also, generalizes the previous quasi-geostrophic result to finite vertical displacements of the interface.

Finally, we briefly explored the instabilities of a buoyant geostrophic current along a coastal wall and with an offshore front. Not surprisingly, we found a similar dependence of the most unstable wavelength on the basic flow parameters (via a Burger number and a depth ratio) to that reported by previous authors from laboratory experiments and oceanographic observations.

The preceding simulations form but a small sample of what can actually be simulated with the PIC method. Because the Coriolis force is computed for each particle at its current site, beta-plane cases can easily be treated by making the Coriolis parameter dependent on the spatial coordinates. Westward drift and Rossby-wave radiation can then be studied for frontal lens-like vortices. Other simulations could be devoted to the stability of lens-like vortices of radial structure other than parabolic. In particular, one could investigate the importance of a relative-vorticity profile that is nonmonotonic in the radial direction (so-called shielded vortices). Still with only minor changes to the code, one could study the formation and development of a buoyant coastal intrusion by initializing the system with no upper layer and steadily injecting buoyant particles in one or several cells along the wall.

Finally, further extensions and generalizations are eminently possible. First, one could remove the quasi-geostrophic (QG) approximation made to the lower layer. This can be done by using an existing finite-difference code for two-dimensional

(barotropic) flow over arbitrary topography, where the topography here happens to be the instantaneous thickness of the upper layer. Likewise, the inclusion of bottom topography, with or without removal of the lower-layer QG approximation, would be straightforward. Extension to more than two layers is also immediate, regardless of how many terminate at intersections of density interfaces within the domain. One simply has to treat all such layers with the PIC approach and all others with a conventional code; coupling between layers will naturally occur in the diagnostic relations extending the geometric constraint (4) and hydrostatic balance (5) to multiple layers. Applications to intermediate-depth Mediterranean salt lenses, bottom lenses, and bottom currents are eminently possible.

Appendix: Extremum Value of the Burger Number

There exists an upper bound on the value of the Burger number for reduced-gravity geostrophic flows with zero coastal velocity and offshore front. To show this, we invoke (1) the geostrophic relation:

$$fv = g' \frac{dh}{dx} \quad (\text{A1})$$

where $v(x)$ is the geostrophic velocity profile, (2) the requirement of inertial stability that the total (planetary + relative) vorticity must have the same sign as the planetary vorticity [Holton, 1992, p. 207]:

$$f \left(f + \frac{dv}{dx} \right) \geq 0 \quad (\text{A2})$$

and (3) the accompanying boundary conditions: $v = 0$, $h = H$ at $x = 0$ (coastal wall) and $v = V$, $h = 0$ at $x = L$ (offshore front). Obviously, the two constants H and L must be positive.

We then multiply $f(f + dv/dx)$ by $(L - x)$, integrate the product over $0 \leq x \leq L$, use (A1) after an integration by parts, and impose the boundary conditions to obtain

$$\int_0^L f \left(f + \frac{dv}{dx} \right) (L - x) dx = \frac{f^2 L^2}{2} - g' H \quad (\text{A3})$$

Because of (A2) and since $(L - x) \geq 0$ over the interval of integration, the integrand is positive, and we find $f^2 L^2 / 2 - g' H \geq 0$, which leads to

$$Bu = \frac{g' H}{f^2 L^2} \leq \frac{1}{2} \quad (\text{A4})$$

Thus the Burger number is at most 1/2. When Bu equals 1/2, (A3) yields that the total vorticity $f + dv/dx$ must be identically zero for all values of x ($0 \leq x \leq L$). Thus the limiting value of the Burger number corresponds to the case of zero potential vorticity. Geostrophic flows for which (A2) is not met are inertially unstable and break down in about one inertial period.

Acknowledgments. This research was made possible by grants of the Office of Naval Research (N00014-93-I-0391) and of the National Science Foundation (OCE-9118426) to Dartmouth College, for which the authors express their sincere appreciation. Pertinent remarks and helpful suggestions from numerous colleagues are also acknowledged.

References

- Adamec, D., and R. L. Elsberry, Response of an intense oceanic current system to cross-stream cooling events, *J. Phys. Oceanogr.*, **15**, 273–287, 1985.
- Arakawa, A., and F. Mesinger, Numerical methods used in atmospheric models, *GARP Publ. Ser.*, **17**, 1–42, 1976.
- Aref, H., Integrable, chaotic, and turbulent vortex motion in two-dimensional flows, *Ann. Rev. Fluid Mech.*, **15**, 345–389, 1983.
- Creswell, G. R., The coalescence of two East Australian Current warm-core rings, *Science*, **215**, 161–164, 1982.
- Cushman-Roisin, B., Linear stability of large, elliptical warm-core rings, *J. Phys. Oceanogr.*, **16**, 1158–1164, 1986.
- Cushman-Roisin, B., On the role of filamentation in the merging of anticyclonic lenses, *J. Phys. Oceanogr.*, **19**, 253–258, 1989.
- Cushman-Roisin, B., and S. Merchant-Both, Elliptical warm-core rings in a two-layer ocean with ambient shear, *J. Phys. Oceanogr.*, **25**, 2011–2024, 1995.
- Cushman-Roisin, B., and B. Tang, Geostrophic turbulence and emergence of eddies beyond the radius of deformation, *J. Phys. Oceanogr.*, **20**, 97–113, 1990.
- Cushman-Roisin, B., W. H. Heil, and D. Nof, Oscillations and rotations of elliptical warm-core rings, *J. Geophys. Res.*, **90**, 11,756–11,764, 1985.
- Cushman-Roisin, B., O. E. Esenkov, and B. J. Mathias, A particle-in-cell method for the solution of two-layer shallow-water equations, *Int. J. Numer. Meth. Fluids*, in press, 1999.
- Esenkov, O. E., Simulations of coastal currents in a two-layer ocean with a particle-in-cell method, M.S. thesis, 88 pages, Dartmouth College, Hanover, N. H., 1994.
- Evans, R. H., K. S. Baker, O. B. Brown, and R. C. Smith, Chronology of warm-core ring 82B, *J. Geophys. Res.*, **90**, 8803–8812, 1985.
- Gill, A. E., and R. W. Griffiths, Why should two anticyclonic eddies merge?, *Ocean Modell.*, **41**, pp. 10–16, Hooke Inst. Oxford Univ., Oxford, England, 1981.
- Griffiths, R. W., and E. J. Hopfinger, Experiments with baroclinic vortex pairs in a rotating fluid, *J. Fluid Mech.*, **173**, 501–518, 1986.
- Griffiths, R. W., and E. J. Hopfinger, Coalescence of geostrophic vortices, *J. Fluid Mech.*, **178**, 73–97, 1987.
- Griffiths, R. W., and P. F. Linden, The stability of buoyancy driven coastal currents, *Dyn. Atmos. Oceans*, **5**, 281–306, 1981.
- Griffiths, R. W., and P. F. Linden, Laboratory experiments on fronts, I, Density-driven boundary currents, *Geophys. Astrophys. Fluid Dyn.*, **19**, 159–187, 1982.
- Griffiths, R. W., and A. F. Pearce, Instability and eddy pairs on the Leeuwin Current south of Australia, *Deep Sea Res.*, **32**, 1511–1534, 1985.
- Hockney, R. W., and J. W. Eastwood, *Computer Simulation Using Particles*, 540 pp., McGraw-Hill, New York, 1988.
- Hogg, N. G., and H. M. Stommel, The heton, an elementary interaction between discrete baroclinic geostrophic vortices, and its implications concerning eddy heat-flow, *Proc. R. Soc. London, Ser. A*, **397**, 1–20, 1985.
- Holton, J. R., *An Introduction to Dynamic Meteorology*, 3rd ed., 507 pp., Academic, San Diego, Calif., 1992.
- Killworth, P. D., and M. E. Stern, Instabilities on density-driven buoyancy currents and fronts, *Geophys. Astrophys. Fluid Dyn.*, **22**, 1–18, 1982.
- Kowalik, Z., J. L. Lueck, and T. C. Royer, On the dynamics of the Alaska Coastal Current, *Cont. Shelf Res.*, **14**, 831–847, 1994.
- Love, A. E. H., On the stability of certain vortex motions, *Proc. London Math. Soc.*, **25**, 18–43, 1893.
- Mathias, B. J., Simulations of vortex evolution and interaction in a two-layer ocean with a particle method, M.S. thesis, 71 pp., Dartmouth College, Hanover, N. H., 1992.
- McClimans, A. T., and J. H. Nilsen, Whirls in the Norwegian Coastal Current, in *Coastal Oceanography*, edited by H. G. Gade, A. Edwards, and H. Svendsen, pp. 311–321, Plenum, New York, 1982.
- McClimans, A. T., Å. Vinger, and M. Mork, The role of the Froude number in models of baroclinic coastal currents, *Ocean Modell.*, **62**, pp. 14–17, Hooke Inst. Oxford Univ., Oxford, England, 1985.
- McWilliams, J. C., The emergence of isolated coherent vortices in turbulent flow, *J. Fluid Mech.*, **146**, 21–43, 1984.
- Melander, M. V., N. J. Zabusky, and J. C. McWilliams, Symmetric vortex merger in two dimensions: Causes and conditions, *J. Fluid Mech.*, **195**, 303–340, 1988.

- Millot, C., Some features of the Algerian Current, *J. Geophys. Res.*, *90*, 7169–7176, 1985.
- Mork, M., Circulation phenomena and frontal dynamics of the Norwegian Coastal Current, *Philos. Trans. R. Soc. London, Ser. A*, *302*, 635–647, 1981.
- Paldor, N., Stability and stable modes of coastal fronts, *Geophys. Astrophys. Fluid Dyn.*, *27*, 217–228, 1983.
- Paldor, N., Amplitude-wavelength relations of nonlinear frontal waves on coastal currents, *J. Phys. Oceanogr.*, *18*, 753–760, 1988.
- Paldor, N., and M. Ghil, Finite-wavelength instabilities of a coupled density front, *J. Phys. Oceanogr.*, *20*, 114–123, 1990.
- Pavia, E. G., and B. Cushman-Roisin, Modeling of oceanic fronts using a particle method, *J. Geophys. Res.*, *93*, 3554–3562, 1988.
- Pavia, E. G., and B. Cushman-Roisin, Merging of frontal eddies, *J. Phys. Oceanogr.*, *20*, 791–814, 1990.
- Polvani, L. M., Two-layer geostrophic vortex dynamics, 2, Alignment and two-layer V-states, *J. Fluid Mech.*, *225*, 241–270, 1991.
- Polvani, L. M., N. J. Zabusky, and G. R. Flierl, Two-layer geostrophic vortex dynamics, I, Upper layer V-states and merger, *J. Fluid Mech.*, *205*, 215–242, 1989.
- Pratt, L. J., and M. E. Stern, Dynamics of potential vorticity fronts and eddy detachment, *J. Phys. Oceanogr.*, *16*, 1101–1120, 1986.
- Richardson, P. L., A. E. Strong, and J. A. Knauss, Gulf Stream eddies: Recent observations in the Sargasso Sea, *J. Phys. Oceanogr.*, *3*, 297–301, 1973.
- Ripa, P., On the stability of elliptical vortex solutions of the shallow-water equations, *J. Fluid Mech.*, *183*, 343–363, 1987.
- Robinson, A. R. (Ed.), *Eddies in Marine Science*, 609 pp., Springer-Verlag, New York, 1983.
- Royer, T. C., Observations of the Alaska Coastal Current, in *Coastal Oceanography*, edited by H. G. Gade, A. Edwards, and H. Svendsen, pp. 9–31, Plenum, New York, 1982.
- Sanson, L. Z., F. Graef, and E. G. Pavia, Collision of anticyclonic, lens-like eddies with a meridional western boundary, *J. Geophys. Res.*, *103*, 24,881–24,890, 1998.
- Schultz-Tokos, K. L., H. H. Hinrichsen, and W. Zenk, Merging and migration of two meddies, *J. Phys. Oceanogr.*, *24*, 2129–2141, 1994.
- Schwarz, H. R., *Numerical Analysis: A Comprehensive Introduction*, 519 pp., John Wiley, New York, 1989.
- Stern, M. E., Geostrophic fronts, bores, breaking and blocking waves, *J. Fluid Mech.*, *99*, 687–703, 1980.
- Sun, S., R. Bleck, and E. P. Chassignet, Layer outcropping in numerical models of stratified flows, *J. Phys. Oceanogr.*, *23*, 1877–1884, 1993.
- Valcke, S., and J. Verron, Interactions of baroclinic isolated vortices: The dominant effect of shielding, *J. Phys. Oceanogr.*, *27*, 524–541, 1997.
- van Ballegooyen, R. C., M. L. Gründlingh, and J. R. E. Lutjeharms, Eddy fluxes of heat and salt from the southwest Indian Ocean into the southeast Atlantic Ocean: A case study, *J. Geophys. Res.*, *99*, 14,053–14,070, 1994.
- Yasuda, I., and G. R. Flierl, Two-dimensional asymmetric vortex merger: Merger dynamics and merger distance, *Dyn. Atmos. Oceans*, *26*, 159–181, 1997.
- Yasuda, I., K. Okuda, and M. Hirai, Evolution of a Kuroshio warm-core ring: Variability of the hydrographic structure, *Deep Sea Res.*, *39*, suppl., S131–S161, 1992.

B. Cushman-Roisin, Thayer School of Engineering, Dartmouth College, Hanover, NH 03755. (Benoit.R.Roisin@Dartmouth.edu)
 O. E. Esenkov, Rosenstiel School of Marine and Atmospheric Science, University of Miami, Miami, FL 33149.

(Received February 18, 1998; revised January 20, 1999; accepted February 11, 1999.)